Title
CX3CR1 mutation alters synaptic and astrocytic protein expression, topographic gradients, and response latencies in the auditory brainstem

Journal
The Journal of Comparative Neurology, 529(11)

ISSN
1550-7149

Authors
Milinkeviciute, Giedre
Chokr, Sima M
Castro, Emily M
et al.

Publication Date
2021-08-01

DOI
10.1002/cne.25150

Peer reviewed

HHS Public Access

Author manuscript

J Comp Neurol. Author manuscript; available in PMC 2022 August 01.

Published in final edited form as:

J Comp Neurol. 2021 August 01; 529(11): 3076–3097. doi:10.1002/cne.25150.

CX3CR1 mutation alters synaptic and astrocytic protein expression, topographic gradients, and response latencies in the auditory brainstem

Giedre Milinkeviciute, **Sima M. Chokr**, **Emily M. Castro**, **Karina S. Cramer**

Department of Neurobiology and Behavior, University of California, Irvine, California

Abstract

The precise and specialized circuitry in the auditory brainstem develops through adaptations of cellular and molecular signaling. We previously showed that elimination of microglia during development impairs synaptic pruning that leads to maturation of the calyx of Held, a large encapsulating synapse that terminates on neurons of the medial nucleus of the trapezoid body (MNTB). Microglia depletion also led to a decrease in glial fibrillary acidic protein (GFAP), a marker for mature astrocytes. Here, we investigated the role of signaling through the fractalkine receptor (CX3CR1), which is expressed by microglia and mediates communication with neurons. *CX3CR1*$^{-/-}$ and wild-type mice were studied before and after hearing onset and at 9 weeks of age. Levels of GFAP were significantly increased in the MNTB in mutants at 9 weeks. Pruning was unaffected at the calyx of Held, but we found an increase in expression of glycinergic synaptic marker in mutant mice at P14, suggesting an effect on maturation of inhibitory inputs. We observed disrupted tonotopic gradients of neuron and calyx size in MNTB in mutant mice. Auditory brainstem recording (ABR) revealed that *CX3CR1*$^{-/-}$ mice had normal thresholds and amplitudes but decreased latencies and interpeak latencies, particularly for the highest frequencies. These results demonstrate that disruption of fractalkine signaling has a significant effect on auditory brainstem development. Our findings highlight the importance of neuron-microglia-astrocyte communication in pruning of inhibitory synapses and establishment of tonotopic gradients early in postnatal development.

Correspondence Karina S. Cramer, Department of Neurobiology and Behavior, University of California, Irvine, CA. cramerk@uci.edu.

AUTHOR CONTRIBUTIONS

The authors take full responsibility for the integrity of the data and accuracy of the analysis. Study concept and design: Giedre Milinkeviciute and Karina S. Cramer. Acquisition of Data: Giedre Milinkeviciute, Emily M. Castro, and Sima M. Chokr. Analysis of data: Giedre Milinkeviciute and Sima M. Chokr. Interpretation of data: Giedre Milinkeviciute, Sima M. Chokr, and Karina S. Cramer. Drafting of the manuscript: Giedre Milinkeviciute, Karina S. Cramer, and Sima M. Chokr.

CONFLICT OF INTEREST

The authors declare no competing financial interests.

PEER REVIEW

The peer review history for this article is available at https://publons.com/publon/10.1002/cne.25150.

DATA AVAILABILITY STATEMENT

Data availability statement: Data will be made available upon request.

SUPPORTING INFORMATION

Additional supporting information may be found online in the Supporting Information section at the end of this article.

Keywords

ABR; astrocytes; auditory brainstem; fractalkine; inhibition; microglia; MNTB; neurotactin; pruning; tonotopy

1 | INTRODUCTION

Microglia are highly dynamic cells that continuously extend their processes to survey the brain parenchyma (Nimmerjahn et al., 2005). Microglia function in immune responses of the brain (Sousa et al., 2017) and have a significant role in neural development (Nelson & Lenz, 2017; Reemst et al., 2016) and construction of neural circuits (Basilico et al., 2019; Miyamoto et al., 2016; Nonaka & Nakanishi, 2019) in normal and pathological conditions (Neniskyte & Gross, 2017; Whitelaw, 2018; Wolf et al., 2017). Microglia eliminate synapses (Paolicelli et al., 2011; Schafer et al., 2012); promote formation of new synapses (Miyamoto et al., 2016; Parkhurst et al., 2013); and participate in synaptic remodeling (Schafer et al., 2012) during development and in synaptic plasticity (Parkhurst et al., 2013; Schafer & Stevens, 2015; Sipe et al., 2016). These functions depend on neuronal activity and on direct contact between microglia and neurons (Wake etal., 2009).

Neuronal communication with microglia occurs in part through fractalkine (CX3CL1), a transmembrane glycoprotein chemokine widely expressed by neurons. It can exist in three forms—membrane-anchored, pro-adhesive, and secreted. CX3CL1 is bound by the receptor CX3CR1, which is expressed by microglia (Harrison et al., 1998; Hatori et al., 2002; Jung et al., 2000). In a *CX3CR1* transgenic mouse line, the *CX3CR1* gene was replaced with the gene encoding the enhanced green fluorescent protein (EGFP) (Jung et al., 2000). This mouse line allows investigation of the effect of fractalkine signaling on the development of neural circuits together with visualization of microglia with the EGFP reporter. *CX3CR1* deficiency was shown to impair the postnatal functional development of thalamocortical synapses in the barrel cortex (Hoshiko et al., 2012). In the olfactory bulb, *CX3CR1* mutation led to the reduction of adult-born-granule cell spine density, dynamics and size (Reshef et al., 2017) while in dentate gyrus, *CX3CR1* deficiency resulted in faulty synaptic integration as well as depletion of synaptic vesicles (Bolos et al., 2018). In contrast, in the visual cortex, loss of *CX3CR1* had no effect on the baseline synaptic turnover or on both early and late forms of activity-dependent visual system plasticity (Lowery et al., 2017).

In the auditory system, the role of fractalkine signaling has been examined only in the cochlea, where CX3CR1 is expressed by macrophages (Kaur et al., 2015) and CX3CL1 is expressed by spiral ganglion neurons (Hirose et al., 2005; Jung et al., 2000). Lack of CX3CR1 resulted in increased loss of spiral ganglion neurons after selective hair cell lesion (Kaur et al., 2015) and after ototoxic or acoustic injury (Kaur et al., 2018). In addition, lack of fractalkine receptor in macrophages impaired the spontaneous recovery of ribbon synapses after acoustic trauma (Kaur et al., 2019). CX3CR1-deficient macrophages stimulated kanamycin ototoxicity in mice (Sato et al., 2010) while promoting hair cell survival and improving hearing function of neomycin-treated mice (Sun et al., 2015). The role of fractalkine signaling in the auditory brainstem has not been identified.

We previously showed that pharmacological depletion of microglia early in development leads to aberrant pruning of calyces of Held in the medial nucleus of the trapezoid body (MNTB). This projection arises from the ventral cochlear nucleus (VCN) and projects contralaterally in brainstem circuitry needed for sound localization. During development, multiple small inputs are eliminated, resulting in a single, encapsulating calyx (Hoffpauir et al., 2006; Holcomb et al., 2013). A single dominant calyceal input on the principal neuron can be seen starting as early as P6 (Holcomb et al., 2013). However, smaller calyces may be still present and around 10% of neurons are continually innervated by multiple calyces (Holcomb et al., 2013; Milinkeviciute et al., 2019). Microglia depletion resulted in retention of polyinnervated MNTB neurons after the onset of hearing, when MNTB neurons are normally monoinnervated. In addition, the expression of glial fibrillary acidic protein (GFAP), a mature astrocyte marker, was decreased in the absence of microglia (Milinkeviciute et al., 2019). These observations, together with the importance of fractalkine for neuron-microglia communication, have led us to investigate the function of fractalkine signaling in auditory brainstem maturation. Here, we tested whether CX3CR1-mediated communication between neurons and microglia is necessary for synaptic and calyceal pruning in MNTB. We found no significant effect of *CX3CR1* mutation on calyceal pruning. MNTB normally displays tonotopic gradients in inputs, cell size, and gene expression patterns. Here, we demonstrate that there is a tonotopic gradient of calyx size as well. However, the tonotopic gradients of calyx size and neuron size were absent in *CX3CR1* mutant mice. *CX3CR1* mutation led to changes in the emergence of mature synaptic proteins, with a significant increase in levels of the glycine transporter (GLYT2). In contrast with our previous results (Milinkeviciute et al., 2019), loss of fractalkine signaling significantly *increased* expression levels of GFAP. Auditory brainstem recordings resulted in significantly shorter latencies at all frequency levels, especially at 32 kHz, highlighting the sensitivity of high-frequency auditory regions in the MNTB to the *CX3CR1* mutation. These results demonstrate that neuron-microglia signaling operates at multiple levels to shape auditory circuitry during postnatal development and highlight the range of microglial function in development.

2 | MATERIALS AND METHODS

2.1 | Animals

We used wild-type (WT) and *CX3CR1*$^{-/-}$ mutant mice of both sexes. *CX3CR1*$^{-/-}$ mutant mice (Jackson Labs Stock Number #005582) were bred on the C57BL/6 background and the generation of the strain has been described in the study by Jung et al. (2000). Seventeen WT mice were used at postnatal day 8 (P8), 33 mice at P14, and 8 mice at 9 weeks of age. Eleven *CX3CR1*$^{-/-}$ mice were used at P8, 33 at P14, and 7 animals at 9 weeks. For auditory brainstem recordings (ABRs), we used 16 WT and 14 *CX3CR1*$^{-/-}$ mice at 9 weeks of age, an age at which hearing is mature (Chang et al., 2018; Sinclair et al., 2017; Sonntag et al., 2009), but the age-related hearing loss that characterizes this background strain has not yet begun (Ison et al., 2007; Ohlemiller et al., 2016). All procedures were approved by the University of California, Irvine Institutional Animal Care and Use Committee.

2.2 | Antibodies and immunohistochemistry

We performed immunofluorescence for vesicular glutamate transporters 1 and 2 (VGLUT1/2), vesicular gamma-aminobutyric acid (GABA) transporter (VGAT), GLYT2, and the astrocytic marker GFAP. Mice were weighed (Figure S1) and perfused transcardially with 0.9% saline followed by 4% paraformaldehyde (PFA) in 0.1 M phosphate buffer, pH 7.3 (PBS). Brainstems were dissected and postfixed in PFA solution overnight. The next day, brains were equilibrated in a 30% sucrose solution in 0.1 M PBS and then sectioned coronally at 18 μm using a cryostat (CM 1850-3-1; Leica Microsystems). For each brainstem, sections were mounted directly on a series of five chrome alum-coated glass slides so that each slide contained every fifth section.

Mounted sections were outlined with a PAP pen hydrophobic barrier and rinsed in 0.1 M PBS for 5 min. For antigen retrieval, tissue was incubated for 5 min in 0.1% sodium dodecyl sulfate in 0.1 M PBS solution then washed in 0.1 M PBS. Sections were then incubated in a blocking solution containing 5% normal goat serum (NGS; Vector Laboratories S-1000) and 0.3% Triton X-100 (Acros 9002-93-1) in 0.1 M PBS for 1 h at room temperature in a humidity chamber. Primary antibodies (Table 1) were diluted in blocking solution, applied to the sections and left to incubate overnight at room temperature in a humidity chamber. The tissue was then rinsed in 0.1 M PBS and incubated for 1 h in goat anti-rabbit Alexa 647 (1:500; Thermo Fisher A21244, AB_2535812) or anti-chicken Alexa 488 secondary antibody (1:200; Thermo Fisher A11039, AB_2534096). Sections were then washed in 0.1 M PBS and incubated in a red or blue fluorescent Nissl stain (NeuroTrace 530/615; Life Technologies N21482 or NeuroTrace 435/455, Life Technologies N21479) diluted in 1:200 in 0.3% Triton X-100 in 0.1 M PBS. After 1 h, tissue was rinsed in 0.1 M PBS and coverslipped with glycergel mounting medium (Dako C0563).

2.3 | Neuronal density

To test for effects of CX3CR1 mutation on cell number, we determined the cell density in MNTB ($N = 5$ WT and 5 *CX3CR1*$^{-/-}$ mice at P8 and 5 WT and 6 *CX3CR1*$^{-/-}$ mice at P14). Tissue prepared for synaptic protein analysis was used for neuronal density analysis. Cells were plotted using images containing blue or red fluorescent Nissl stain. Fiji's "Cell Counter" was used to count neurons within the outlined region of interest (ROI) of each MNTB section. Five MNTB sections from either left or right side were used per animal. Principal neurons of the MNTB were identified as homogenous cells that were round or slightly oval in shape (Hoffpauir et al., 2006; Weatherstone et al., 2017). Only neuronal bodies with a visible nucleus and nucleolus were counted. If a neuron was located at the border of the ROI, it was included in the count only if at least half of the soma was within that ROI. Neuronal density was calculated by dividing the sum of neuronal counts from each MNTB by the sum of MNTB area in the slices used for analysis.

2.4 | Fluorescent microscopy and areal coverage analysis

We acquired 20× magnification images of sections throughout the rostrocaudal extent of the MNTB using a Zeiss Axioskop-2 microscope, an Axiocam camera, and Axiovision software. Both MNTBs were analyzed. Animals in which at least three intact sections of MNTB were present were included in the study.

Image analysis was performed as previously described (Milinkeviciute et al., 2019; Schrode et al., 2018) by two examiners, blind to genotype, and their results were averaged. Briefly, a series of 20× multichannel fluorescent photographs spanning the rostrocaudal extent of the MNTB was assembled as an image stack in FIJI (Schindelin et al., 2012) for each animal. The boundary of the MNTB was outlined in each section using the photograph taken with channel corresponding to Nissl staining. For the outline, we used the ROI polygon function in FIJI. All subsequent operations were performed on the image channel corresponding to the immunolabeling of interest (e.g., GLYT2). Additionally, we drew and stored an ROI vector that estimated the direction of the tonotopic axis of the MNTB in each section from the most medial to the most lateral point of the MNTB (approximately parallel to the mediolateral axis). Optical density for each section containing the labeling of interest was evaluated across three compartments—medial, central, and lateral—that spanned the estimated tonotopic axis of the MNTB. Compartment locations were determined by computing the orthogonal projection of the MNTB ROI polygon onto the estimated tonotopic vector and subdividing the resulting region of overlap into three equally sized line segments. The line segment closest to the midline designated the medialmost compartment, and each compartment encompassed all pixel data orthogonal to its line segment. The areal coverage ratio was quantified as the total number of thresholded pixels within a given compartment across all sections divided by the total number of pixels within the entire MNTB ROI intersecting a given compartment across all sections. With the exception of manual drawing of the MNTB border and tonotopic vector, all steps were fully automated, thus minimizing the possibility of experimenter bias.

To visualize GLYT2 staining across VCN, LSO, and MNTB, 10× magnification images were acquired and stitched together using Photoshop. Histograms of Nissl and GLYT2 staining were adjusted to achieve the clearest and best visual representation of immunolabeling. Both genotype groups contained a negative control in which the primary antibody was omitted during the immunolabeling process.

2.5 | Axon tracing

In 19 animals at P14, we performed neuronal tracing to fill calyces of Held in the MNTB. Mice were perfused transcardially with artificial cerebrospinal fluid (aCSF; 130 mM NaCl, 3 mM KCl, 1.2 mM KH_2PO_4, 20 mM NaHCO3, 3 mM HEPES, 10 mM glucose, 2 mM CaCl2, 1.3 mM MgSO4 perfused with 95% O_2 and 5% CO_2). Brains were quickly dissected and placed in a chamber with oxygenated aCSF. Axonal projections from the anteroventral VCN (AVCN) to the MNTB were filled using a pulled glass micropipette filled with rhodamine dextran amine (RDA; MW 3000, Invitrogen) solution (6.35% RDA with 0.4% Triton-X100 in PBS), which was then electroporated (Electro Square Porator (ECM830; BTX) with 5 pulses per second (pps) at 55 V for 50 ms into the ventral acoustic stria close to the midline. These pulses resulted in sparse labeling of globular bushy cell (GBC) axons and their terminal calyces of Held on both sides of the brainstem. The brain was then placed back into the aCSF chamber for approximately 2 h under continuous oxygenation to allow for dye transport. The tissue was then transferred to 4% PFA solution for another 2 h followed by incubation in 30% sucrose solution in 0.1 M PBS. Brainstems were cryosectioned in the coronal plane at 18 μm and mounted on an alternating series of five

slides. Slides with adequately labeled axons and calyces of Held were immunolabeled for VGLUT1/2 as described above.

2.6 | Confocal microscopy

RDA-labeled and VGLUT1/2-labeled tissue from 11 WT and 8 *CX3CR1*$^{-/-}$ P14 mice was used for confocal microscopy (Leica SP8; 63× oil objective, zoom: 1.5, pinhole: 1) and subsequent analysis. Nissl, RDA, and VGLUT1/2 z-stack images of calyces of Held were acquired at a resolution of 1024 × 1024 pixels, with a z-step size of 0.5 μm. Gain and offset were set for each fluorescent channel and each slide separately. In a few instances, these settings were adjusted to account for differences in labeling intensity between sections on the same slide. Image stacks were exported and surface area and volume of calyces of Held were analyzed using the surface module in Imaris software (v9.5.0 and v9.3.0; Bitplane). RDA electroporation resulted in random labeling of calyces throughout the MNTB. Therefore, the entire mediolateral extent of the MNTB was analyzed. Surfaces of RDA-labeled calyces of Held were reconstructed using smoothing and background both set to 0.4 μm and then manually adjusted to optimize rendering of the labeled calyx. Sections were coded and analyzed blind to genotype. Only one slide per animal was analyzed and complete or near complete RDA-filled calyces of Held with visibly preterminal axon segments were included in the analysis. Any RDA-labeled calyces that were not possible to individually reconstruct were excluded from the analysis. If the number of RDA-filled calyces from one slide was less than 5, results from such animal were excluded from any calyceal quantitative analyses. Smoothing and background function settings were 1.7 μm and 10 μm, respectively. Neurons and calyx of Held numbers analyzed and included in the study from WT and *CX3CR1*$^{-/-}$ cohorts are reported in Table 2.

2.7 | Determination of monoinnervation

At the time of surface rendering, the monoinnervation or polyinnervation status of the postsynaptic neuron was evaluated as previously described (Milinkeviciute et al., 2019). Briefly, RDA-labeled brainstems from WT and *CX3CR1*$^{-/-}$ P14 mice were stained for VGLUT1/2 and MNTB neurons receiving an RDA-filled input were analyzed. Some neurons were contacted by an RDA-filled calyx of Held while others, in addition to the RDA-labeled calyx, showed VGLUT1/2 labeling outside of the calyx in close proximity to the neuronal soma. This VGLUT1/2 labeling was indicative of additional calyceal input onto the same MNTB neuron. We thus set our criteria such that VGLUT1/2 labeling outside of the calyx that was continuous and contacted no less than 25% of the neuronal surface was considered additional calyceal input and the neuron was classified as polyinnervated. Percentages of monoinnervated and polyinnervated neurons are presented in Table 2.

2.8 | Calyx of Held size along the mediolateral axis of MNTB

We plotted all RDA-labeled and reconstructed calyces of Held along the mediolateral axis of MNTB. We acquired 20× magnification images of sections that were used for confocal analysis using a Zeiss Axioskop-2 microscope, an Axiocam camera, and Axiovision software. We outlined the MNTB and defined an axis from the medialmost to the lateralmost point of the MNTB in FIJI. The location of each of the reconstructed calyces was calculated along this mediolateral MNTB axis. We used a simple linear regression to investigate the

correlation between the surface area of calyces of Held and their positions in MNTB and determined whether there was a significant difference between the WT and *CX3CR1*$^{-/-}$ correlation coefficients. In addition, MNTB was subdivided into two or three equal bins, 0% −50% and 50%−100% and medial, central, and lateral, respectively. The average surface area of calyx of Held was calculated for each of these bins.

The volume of each of the reconstructed calyces of Held was measured, and, together with the surface area, was used to calculate the calyceal shape factor. A shape factor was calculated as $(SA1.5)/(6\sqrt{\pi V})$, where SA is the surface area of the calyx and V is its volume (deHoff, 1978; Muniak et al., 2018). This shape factor represents the intricate branching of the calyx of Held. The larger the shape factor, the more complex the calyx of Held; a shape factor of 1.0 characterizes a perfect sphere. The analysis was performed blind to the genotype.

2.9 | Neuron cross-sectional area measurement

Three WT and three *CX3CR1*$^{-/-}$ mice at P14 and 9 weeks were used to measure neuronal cross-sectional areas. Confocal images of Nissl-stained tissue were taken with a Leica SP8 63× oil objective. Images were acquired at a resolution of 1024 × 1024 pixels, with a z-step size of 1 μm (speed; 600, line average: 2, pinhole; 1). An image of the entire MNTB was acquired using the Tiling function. A different number of z-stacks were needed for each MNTB photographed. Separate z-stacks were stitched together using Imaris Stitch (9.5.0.). These composite images were then used to make maximum projection images in FIJI. We outlined and measured the MNTB and principal neurons within that MNTB using a polygon tool. Only neurons with a visible nucleus and nucleolus were measured. Additionally, neurons at the MNTB boundary were excluded. Cross-sectional area averages of all neurons measured in WT and *CX3CR1*$^{-/-}$ group were compared.

2.10 | Neuron cross-sectional area plotting along the mediolateral MNTB axis

MNTB tonotopic arrangement follows the mediolateral axis, with high and low frequencies located in the medial and lateral MNTB, respectively (Sommer et al., 1993; Tolnai et al., 2008). A neuronal size gradient has been demonstrated in MNTB (Rotschafer & Cramer, 2017; Weatherstone et al., 2017). We measured X coordinates of the most medial and the most lateral point of the MNTB ROI in FIJI and plotted measured neurons along the mediolateral axis. Correlation between the location and cross-sectional area of each neuron from WT and *CX3CR1*$^{-/-}$ group and significance of the difference between the correlation coefficients were calculated using linear regressions.

2.11 | Auditory brainstem response recording

ABRs were performed on mice at 9 weeks. The recordings of WT and CX3CR1$^{-/-}$ mice were interleaved and the same stimulus file was used throughout the experiment. Mice were anesthetized with an intramuscular injection of ketamine (75 mg/kg, KetaVed, VEDCO) and xylazine (15 mg/kg, AnaSed, NADA # 139–236). Body temperature was regulated using a far infrared warming pad (35°C; 15.2 cm W × 20.3 cm L, Kent Scientific, RT-0501), which was positioned on a Kopf model 900 Small Animal stereotaxic frame. Pin electrodes were inserted subcutaneously with the positive electrode in the vertex, the negative electrode

placed at the right cheek, and the ground electrode in the back near the right leg. Electrodes were connected to a Tucker-Davis Technologies (TDT) RA4PA 4-channel Medusa amplifier, which connected to a TDT RA16 Medusa Base Station.

ABRs were performed in a sound-attenuating chamber (102 cm × 98 cm × 81 cm, Industrial Acoustics Company). Sound stimuli were generated using TDT SigGen software version 4.4 and were presented 500 times at a rate of 21 stimuli per second. Sound was presented using TDT MF1 Multi-Function Speaker through an ear tube placed in the animal's left ear. Sound stimuli were emitted via a TDT RP2.1 enhanced real-time processor and signal level was controlled using a TDT PA5 programmable attenuator. Recorded responses were amplified by a TDT SA1 stereo power amp and filtered with the control of BioSig software version 4.4. All responses to sound stimuli were recorded for 12 ms with sound level decreasing in 5 dB SPL steps from 80 to 10 dB SPL. ABRs were first recorded in response to 100 μs click stimuli followed by 4, 8, 12, 16, 24, and 32 kHz tone stimuli. At each sound level, sample responses were averaged to attain an averaged response.

2.12 | ABR analysis

Click and pure tone thresholds were determined by an observer blind to genotype. Threshold was defined as the lowest sound intensity (dB SPL) level at which a recognizable waveform would be detected. Peaks and troughs were manually scored on BioSig by a blind observer, and raw files were extracted from BioSig for further statistical analysis. Peak latency was determined as the time from sound onset (0 ms) to the time of peak apex (ms). Interpeak latency was calculated as the difference in time (ms) between the highest levels of each of the peaks (I-II, II-III, III - IV, I-III, and I - IV). Peak amplitude was calculated as the difference (μV) between the preceding trough and the apex of the relative peak. Genotype differences and interactions of genotype and intensities were calculated with two-way ANOVA analysis, followed by Sidak's multiple comparisons test to determine any intensity-specific differences.

2.13 | Experimental design and statistical analysis

To account for variability among litters, multiple litters were used for each cohort. Quantitative results for all cell counts, calyx of Held sizes, and innervation status as well as coverage of positive immunohistochemistry, neuronal cross-sectional area and ABR analyses are represented by mean scores ± standard error of the mean (SEM) and were analyzed using Prism Software (v8.3.0; GraphPad Software). Comparisons between different treatment and age groups were made using an appropriate *t*-test, one-way, or two-way ANOVA. Post hoc analysis was performed using Sidak's multiple comparisons tests unless otherwise indicated. Statistical significance was accepted at $p < .05$. Degrees of freedom (DF) are presented after each statistical calculation in Section 3. Animal numbers, mean scores ±SEM, as well as effect of genotype are presented in Tables S1 and S2.

3 | RESULTS

3.1 | Effects of *CX3CR1* mutation on synaptic protein expression

We evaluated the effects of loss of *CX3CR1* on the development of excitatory and inhibitory synapses in MNTB using synaptic markers. To examine the presence of excitatory terminals, we used immunofluorescence to label VGLUT1/2 (Fremeau et al., Fremeau Jr. et al., 2001; Herzog et al., 2001; Kaneko et al., 2002). Inhibitory terminals were evaluated using VGAT and GLYT2 immunofluorescence (McIntire et al., 1997; Wang et al., 2009).

VGLUT1/2 labeling in the MNTB of mature animals nearly completely surrounds each of the principal neurons, reflecting the presence of the large, excitatory calyces of Held that contact these neurons (Borst & Soria van Hoeve, 2012; Forsythe, 1994; Kuwabara et al., 1991). Tissue from WT and $CX3CR1^{-/-}$ mice was immunolabeled with VGLUT1/2 and analyzed for areal coverage ratio of immunopositive labeling in the MNTB at P8 (WT P8: 0.2 ± 0.01, $N = 15$; $CX3CR1^{-/-}$ P8: 0.13 ± 0.01, $N = 7$; Figure 1(a,b)) and P14 (WT P14: 0.18 ± 0.01, $N = 9$; $CX3CR1^{-/-}$ P14: 0.17 ± 0.01, $N = 14$; Figure 1(c,d)). $CX3CR1^{-/-}$ mice had significantly smaller VGLUT1/2 areal coverage ratios than their age-matched WT controls at P8 (WT- $CX3CR1^{-/-}$ P8: $p < .0001$, DF = 41; ANOVA). In the higher magnification images, it was noted that WT calyces almost completely surrounded MNTB neurons, while in mutant mice, the VGLUT1/2 ring was largely incomplete (Figure 1(a1,b1)). VGLUT1/2 expression significantly increased with age only in $CX3CR1^{-/-}$ MNTB (WT P8-P14: $p = .1012$, DF = 41; $CX3CR1^{-/-}$ P8-P14: $p = .0184$, DF = 41; ANOVA) and became comparable to WT expression by P14 (WT-$CX3CR1^{-/-}$ P14: $p = .9410$, DF = 41; ANOVA; Figure 1(e)). These quantitative results were reflected in higher magnification images (Figure 1(c1,d1)) showing VGLUT1/2 immunolabel located around most of the neuronal circumference in both, WT and mutant animals at P14.

Inhibitory currents in MNTB were shown to contain GABAergic and glycinergic components (Awatramani et al., 2005; Mayer et al., 2014). However, GABA contribution to the total inhibition in MNTB declines with age and becomes minor in adult animals (Awatramani et al., 2005). We used VGAT immunofluorescence to label presynaptic inhibitory puncta in MNTB. VGAT is a marker for GABA- and GLYT2-positive terminals as it functions in the uptake of both neurotransmitters into synaptic vesicles (Chaudhry et al., 1998; Wang et al., 2009). We examined VGAT areal coverage ratio in the MNTB at P8 (WT P8: 0.18 ± 0.01, $N = 16$; $CX3CR1^{-/-}$ P8: 0.17 ± 0.01, $N = 10$; Figure 1(f,g)) and at P14 (WT P14: 0.11 ± 0.01, $N = 12$; $CX3CR1^{-/-}$ P14: 0.14 ± 0.01, $N = 14$; Figure 1(h,i)). There were no significant differences in VGAT areal coverage between WT and $CX3CR1^{-/-}$ animals at P8 or P14 (WT-$CX3CR1^{-/-}$ P8: $p = .7795$, DF = 48; WT-$CX3CR1^{-/-}$ P14: $p = .0603$, DF = 48; ANOVA). However, in WT mice, VGAT expression significantly declined with age, while age did not have an effect on VGAT expression in mutant mice (WT P8-P14: $p < .0001$, DF = 48; $CX3CR1^{-/-}$ P8-P14: $p = .0866$, DF = 48; ANOVA; Figure 1 (j)). Thus, lack of fractalkine signaling impairs the age-related decrease of VGAT expression.

We measured the neuronal density in the MNTB of mice of both genotypes at P8 and P14 (WT P8: 0.002 ± 0.0001, $N = 5$; $CX3CR1^{-/-}$ P8: 0.002 ± 0.00008, $N = 5$; WT P14: 0.001 ± 0.00003, $N = 5$; CX3CR1$^{-/-}$ P14: 0.002 ± 0.00006, $N = 6$; Figure 1(k)). Five MNTB

sections per animal from a total of five mice per group (with the exception of *CX3CR1*$^{-/-}$ P14 group where $N = 6$) were used for cell plotting. There was no significant difference found between genotypes at any age tested (*WT-CX3CR1*$^{-/-}$ P8: $p = 0.3853$, DF = 17; *WT-CX3CR1*$^{-/-}$ P14: $p = .7652$, DF = 17). However, we found a significant age-related decrease in neuronal density in both WT and *CX3CR1*$^{-/-}$ mice (WT P8-P14: $p = .0001$, DF = 17; *CX3CR1*$^{-/-}$ P8-P14: $p < .0001$, DF = 17; ANOVA; Figure 1(k)). Thus, any changes observed in VGLUT1/2 and VGAT areal coverage ratios are not due to the difference in neuronal numbers.

MNTB neurons are glycinergic (Kuwabara & Zook, 1991; Tollin, 2003) and principal MNTB neurons are themselves targeted by glycine-positive terminals arriving mainly from the ventral nucleus of trapezoid body (VNTB) (Albrecht et al., 2014; Kuwabara et al., 1991; Thompson & Schofield, 2000). GLYT2 packages glycine neurotransmitter into synaptic vesicles; thus, to selectively examine glycinergic terminals in MNTB, we next investigated the expression of GLYT2 (Armsen et al., 2007; Liu et al., 2001). Upon qualitative observation, GLYT2 expression appeared slightly more intense in mutant than WT mice at P8. In addition, in the medial part of MNTB the GLYT2 expression appeared more dense in *CX3CR1*$^{-/-}$ mice than in WT mice at P8 (Figure 2(a,b)). At P14, GLYT2 staining was more pronounced within MNTB neurons in both genotype groups. However, *CX3CR1*$^{-/-}$ MNTB appeared to maintain more GLYT2-positive fibers and terminals than observed in WT MNTB in addition to the inside of neuronal somata (Figure 2(c,d)). In WT animals, the location of GLYT2 expression in MNTB changed with age from mainly fibers and inputs to neuronal somata at P8 and P14, respectively (Figure 2(a,b)). There was no significant difference in GLYT2 areal coverage between WT and *CX3CR1*$^{-/-}$ mice at P8 (WT-*CX3CR1*$^{-/-}$ P8: $p = .3542$, DF = 43; ANOVA; Figure 2(e)). By P14, GLYT2 areal expression decreased in the WT group (WT P8-P14: $p = .0029$, DF = 43; ANOVA), but not in mutant mice (*CX3CR1*$^{-/-}$ P8-P14: $p = .1172$, DF = 43; ANOVA). At P14, there was significantly greater GLYT2 expression in *CX3CR1*$^{-/-}$ mice than in WT controls (WT-*CX3CR1*$^{-/-}$ P14: $p < .0058$, DF = 43; ANOVA; Figure 2(e)).

We next investigated whether our observed increase in GLYT2 expression in *CX3CR1*$^{-/-}$ mice varied along the tonotopic axis (Figure 2(f)). The MNTB of WT and mutant mice was separated into three bins: medial, central, and lateral. We found that in WT mice, there was significantly less GLYT2 coverage in medial MNTB than in lateral MNTB (WT medial-lateral: $p = .0086$, DF = 66; ANOVA). Similarly, in *CX3CR1*$^{-/-}$ mice, GLYT2 coverage was significantly smaller in the medial than central and lateral MNTB (*CX3CR1*$^{-/-}$ medial-central: $p = .0003$, DF = 66; medial-lateral: $p < .0001$, DF = 66; ANOVA). When GLYT2 levels were compared in each third of MNTB, we found a significant increase in GLYT2 expression only in the central MNTB of the mutant mice when compared to their age-matched controls (WT-*CX3CR1*$^{-/-}$ central: $p = .0067$, DF = 66; ANOVA). Thus, the loss of fractalkine signaling does not affect the gradient of GLYT2 expression. Given the observed changes in GLYT2 levels at P14 (Figure 2(e)), we next examined GLYT2 expression at 9 weeks (Figure 2(g,h)). Five WT and 5 *CX3CR1*$^{-/-}$ mice were used for the study. We observed slight differences in GLYT2 expression between WT and *CX3CR1*$^{-/-}$ mice in the auditory brainstem. Qualitative observations revealed weaker and more diffuse GLYT2 staining in the MNTB of WT mouse (Figure 2(g1)) when compared to the mutant mouse

where GLYT2-positive puncta seemed to form aggregates (Figure 2(h1)). In contrast, GLYT2 immunolabeling was very dense in the LSO and VCN of the WT animal (Figure 2(g2,g3)) when compared to the mutant tissue where it appeared sparser (Figure 2(h2,h3)).

3.2 | *CX3CR1* mutants show enhanced GFAP expression in MNTB

The astrocytic marker GFAP is considered a late-appearing mature astrocyte marker (Gomes et al., 1999). Because GFAP expression is minimal in the MNTB at P8 (Dinh et al., 2014; Milinkeviciute et al., 2019), we examined GFAP expression at P14 weeks (11 WT and 15 *CX3CR1*$^{-/-}$) and 9 weeks (6 WT and 6 *CX3CR1*$^{-/-}$; Figure 3). At P14, GFAP staining was found throughout the MNTB in both, WT and mutant mice. Qualitative GFAP labeling examination revealed slightly more dense expression levels in MNTB of mutant than control mice (Figure 3(a,b)). A clearer difference was observed at 9 weeks, with GFAP less abundant in control MNTB than in that of *CX3CR1*$^{-/-}$ mice (Figure 3(c,d)). In WT animals, GFAP expression decreased at 9 weeks relative to P14, while in mutant animals, the age-related decrease in GFAP expression was less obvious (Figure 3(b,d)). Tissue was analyzed for areal immunofluorescence coverage as described for synaptic proteins. High levels of GFAP expression were observed in WT and *CX3CR1*$^{-/-}$ MNTB in both age groups (WT P14: 0.05 ±0.002, $N = 11$; *CX3CR1*$^{-/-}$ P14: 0.06 ± 0.003, $N = 15$; WT 9 weeks: 0.03 ± 0.002, $N = 6$; *CX3CR1*$^{-/-}$ 9 weeks: 0.05 ± 0.006, $N = 6$; Figure 3(e)). The GFAP-labeled area in *CX3CR1*$^{-/-}$ MNTB was greater but not significant than that measured in the control group at P14 ($p = .0902$, DF = 34). At 9 weeks, GFAP areal coverage ratio was significantly higher in the mutant group than in WT ($p = .0208$, DF = 34). GFAP expression significantly decreased with age in WT and *CX3CR1*$^{-/-}$ MNTB (WT: $p = .0006$, DF = 34; *CX3CR1*$^{-/-}$: $p = .0218$, DF = 34). Thus, disruption of fractalkine-dependent signaling pathway between microglia and neurons significantly increased GFAP expression but did not affect age-related changes of GFAP expression.

3.3 | Effects of disrupted fractalkine signaling on pruning and size gradient of calyces of Held

Calyces of Held were sparsely labeled with RDA. After sectioning, tissue was stained for VGLUT1/2, which in the MNTB largely corresponds to the excitatory calyces of Held. RDA labeling, appearing as a filled volume, together with punctate VGLUT1/2 immunofluorescence enabled us to distinguish monoinnervated from polyinnervated MNTB neurons (Figures 4 and 5). We previously confirmed this method using a double dye electroporation technique to demonstrate that multiple calyces can innervate a single MNTB cell, consistent with observations that around 10% of neurons are continually innervated by multiple calyces neurons (Bergsman et al., 2004; Holcomb et al., 2013; Milinkeviciute et al., 2019; Wimmer et al., 2004). We focused on P14, as our previous study showed that most MNTB neurons were monoinnervated by this age (Milinkeviciute et al., 2019). We found examples of polyinnervated neurons in MNTB of WT mice at P14 (Figure 4 (a,b)). Occasionally, VGLUT1/2-positive input outside of the RDA-labeled calyx had also a visible axon (Figure 4(a)). In some cases, we observed 2 RDA-filled calyces with discernible axons synapsing on a single principal neuron (Figure 4(b)). Similar instances were also detected in *CX3CR1*$^{-/-}$ mice (Figure 4(c,d)). In both genotypes, we found monoinnervated and polyinnervated neurons with calyces of Held exhibiting intricate branching (Figure 5(a-d)).

We calculated the percentage of neurons contacted by more than one calyx (VGLUT1/2 staining in addition to the RDA-positive terminal; Figure 5(c,d)) in the MNTB of WT and *CX3CR1*$^{-/-}$ mice at P14 (WT P14: 16.41 ± 3.56, $N = 11$; *CX3CR1*$^{-/-}$ P14: 15.53 ± 4.81, $N = 8$; Figure 5(e)). We found no significant difference in polyinnervation of MNTB neurons after hearing onset, indicating that a lack of fractalkine signaling does not impair calyceal pruning early in development (WT-*CX3CR1*$^{-/-}$ P14: $p = .8849$, $t = 0.1474$; DF = 13.85; Welch's *t*-test). A small percentage of MNTB neurons were still polyinnervated after hearing onset in WT and *CX3CR1*$^{-/-}$ mice (WT P14:16.41 ± 3.56, $N = 11$; *CX3CR1*$^{-/-}$ P14: 15.53 ± 4.81, $N = 8$).

We next examined the distribution of calyx size along the tonotopic axis of MNTB in P14 animals. We plotted measured surface area of calyces of Held by their location along the mediolateral axis in three MNTB sections per animal from three WT and three *CX3CR1*$^{-/-}$ mice at P14. We found a significant correlation between the surface area and the location of the calyx of Held in WT mice. Smaller calyces were localized to more medial parts of the MNTB and larger calyces were found more laterally (WT P14: Spearman $r = .3039$, $p = .004$, N of XY pairs = 88; Figure 5(f)). This correlation disappeared in *CX3CR1*$^{-/-}$ mice (*CX3CR1*$^{-/-}$ P14: Spearman $r = -.1642$, $p = .1406$, N of XY pairs = 82; Figure 5(g)). The difference between the WT and *CX3CR1*$^{-/-}$ correlation coefficients was significant ($p = .0021$, calculated using http://vassarstats.net/rdiff.html).

We calculated the shape factor of calyces of Held, a measure of complexity related to surface area and volume, in WT and *CX3CR1*$^{-/-}$ mice (Bogaerts et al., 2009; Muniak et al., 2018). There was no difference observed between the shape factor between the two genotypes (WT: 7.45 ± 0.35, $N = 11$; *CX3CR1*$^{-/-}$: 7.08 ± 0.41, $N = 8$; $p = .5056$, $t = 0.6816$; DF = 15.32; Welch's *t*-test; Figure 5(h)).

We subdivided the MNTB in the medial, central, and lateral parts. In WT animals, calyces of Held were significantly larger in the central and lateral MNTB when compared to the those located in the medial part, confirming the tonotopic calyx size gradient across the MNTB (WT medial vs. central: $p = .0011$, DF = 164; medial vs. lateral: $p = .0016$, DF = 164; ANOVA; Figure 5(i)). In *CX3CR1*$^{-/-}$ mice calyces were significantly larger in the central MNTB than in the lateral MNTB (*CX3CR1*$^{-/-}$ central vs. lateral: $p = .0448$, DF = 164; ANOVA). We found that calyces did not differ in size between control and mutant mice in any of the subdivisions (WT-*CX3CR1*$^{-/-}$ medial: $p = .0905$, DF = 164; central: $p = .2862$, DF = 164; lateral: $p = .7861$, DF = 164; ANOVA; Figure 5(i)). This observation may be due to the uneven or limited number of calyces analyzed when subdivided. When MNTB was divided in half, the calyces in the medial half were significantly larger in WT than mutant mice (WT-*CX3CR1*$^{-/-}$ medial half: $p = .0234$, DF = 166; lateral half: $p = .9492$, DF = 166; ANOVA; Figure 5 (j)). Thus, the loss of fractalkine signaling disrupts the size gradient of calyces of Held due to the presence of larger calyces in the medial portion of the MNTB.

3.4 | *CX3CR1* mutation disrupts neuronal size gradient in MNTB

Principal neurons display a size gradient along the tonotopic axis of the MNTB, with smaller neurons and larger neurons located in the lateral and medial ends of the MNTB, respectively (Rotschafer & Cramer, 2017; Weatherstone et al., 2017). We examined the effect of

fractalkine signaling on the gradient of neuronal cross-sectional area along the mediolateral MNTB axis. We limited our analysis to P14 and 9 weeks, when the size gradient is mature (Rotschafer & Cramer, 2017; Weatherstone et al., 2017). We found a significant positive correlation between the neuronal cross-sectional area and its mediolateral position in the MNTB in WT mice at P14 (Spearman $r = .2360$, $p < .0001$, N of XY pairs = 449; Figure 6(a)). Smaller neurons were located medially and gradually increased in size moving toward the lateral part. However, the correlation was negative and the gradient was almost absent in *CX3CR1*$^{-/-}$ mice at P14 (Spearman $r = -.0846$, $p = .0501$, N of XY pairs = 537; Figure 6(b)). There was a significant difference between the WT and *CX3CR1*$^{-/-}$ correlation coefficients ($p < .0001$, calculated using http://vassarstats.net/rdiff.html). Neurons were significantly smaller in medial, central and lateral parts of MNTB of WT mice when compared to *CX3CR1*$^{-/-}$ at P14 (medial: $p < .0001$, DF = 980; central: $p < .0001$, DF = 980; lateral: $p = .005$, DF = 980; ANOVA; Figure 6(c)). At 9 weeks, the correlation between the neuronal cross-sectional area and its position in the MNTB in WT remained positive and significant (Spearman $r = .5634$, $p < .0001$, N of XY pairs = 688; Figure 6(d)). Interestingly, in 9-week-old mutant mice the correlation became positive and significant (Spearman $r = .3315$, $p < .0001$, N of XY pairs = 646; Figure 6(e)); however, a significant difference in correlation coefficients between WT and *CX3CR1*$^{-/-}$ mice remained at 9 weeks ($p < .0001$). At 9 weeks, as at P14, neurons were significantly smaller in medial, central, and lateral portions of MNTB of WT mice when compared to *CX3CR1*$^{-/-}$ (medial: $p < .0001$, DF = 1328; central: $p < .0001$, DF = 1328; lateral: $p = .0267$, DF = 1328; ANOVA; Figure 6(f)). Thus, fractalkine signaling has an effect on neuronal size and its gradient in MNTB, especially early in development.

3.5 | *CX3CR1* mutation reduces latencies of ABR waves

We examined auditory phenotypes by measuring ABRs in 16 WT and 14 *CX3CR1*$^{-/-}$ mice at 9 weeks of age. Peak I reflects activity in the VIIIth nerve, followed by peak II that shows activity in the cochlear nucleus. Peak III corresponds to activity of the superior olivary complex, followed by peak IV showing activity in the lateral lemniscus (Henry, 1979; Jewett et al., 1970; Jewett & Williston, 1971; Picton et al., 1974). Click and pure tone stimuli were presented to the left ear at decreasing intensities from 80 to 10 dB SPL in 5 dB SPL steps. Pure tones were presented at 8, 12, 16, 24, and 32 kHz. Some, but not all, animals were also presented a 4 kHz stimulus ($N = 6$ WT, $N = 9$ *CX3CR1*$^{-/-}$). Click and pure tone traces were analyzed for threshold. Pure tone traces at all intensities were analyzed for absolute peak latency, inter-peak latency, and peak amplitude. Threshold was determined as the lowest intensity at which a recognizable waveform could be observed. Consistent with previous studies (Kaur et al., 2019), *CX3CR1*$^{-/-}$ mice displayed normal hearing threshold in response to click stimuli ($p = .59$; Welch's t test, $t = .6368$, DF = 27.28; Figure 7(a)) but effects of genotype showed significantly lower thresholds in response to pure tones ($p = .0076$, DF = 1, ANOVA). Multiple comparisons tests for pure tones did not show frequency-specific differences (4 kHz: $p = .9602$, DF = 153; 8 kHz: $p = .9439$, DF = 153; 12 kHz: $p = .8448$, DF = 153; 16 kHz: $p = .9037$, DF = 153; 24 kHz: $p = .6662$, DF = 153; 32 kHz: $p = .4770$, DF = 153; ANOVA; Figure 7(b)). All statistical values for peak amplitudes, latencies, and inter-peak latencies are reported in Table S2.

Absolute peak latency was defined as the time (ms) of the highest level (μV) for each peak following the onset of sound (0 ms) (Figure 8 (a)). Two-way ANOVA analysis revealed a main effect of genotype in response to frequencies from 8 to 32 kHz frequency levels, showing significantly reduced peak I-IV latencies in *CX3CR1*$^{-/-}$ mice (Figure 8(b-f); Table S2). Post hoc comparisons showed that Peaks III and IV latencies were significantly reduced in *CX3CR1*$^{-/-}$ mice at some intensity levels at the highest frequencies. These results show that *CX3CR1*$^{-/-}$ mice exhibit faster sound-processing conduction, especially at high frequencies.

To determine central conduction effects of CX3CR1 depletion, interpeak latency was determined by observing the time (ms) between the apex of each peak relative to the following peak, and the apex of Peak I to the subsequent peaks (Figure 8(a)). *CX3CR1*$^{-/-}$ mice showed significantly decreased interpeak latencies between Peaks I and II at 8–32 kHz; however, multiple comparison analyses did not reveal intensity-specific differences (Figure 9(a)). Disrupted fractalkine signaling resulted in significantly decreased Peaks II-III latency at 12, 16, and 32 kHz (genotype effect), but pairwise comparisons did not reach significant at specific intensities (Figure 9(b)). Peaks III-IV latencies were significantly reduced at 8, 12, and 32 kHz in *CX3CR1*$^{-/-}$, with some significant reductions at specific intensities (Figure 9(c)). *CX3CR1*$^{-/-}$ mice showed significantly decreased latencies between Peaks I-III at all frequency levels, with some intensity-specific differences (Figure 9(d)). Peaks I-IV interpeak latencies were significantly decreased at 8–32 kHz in *CX3CR1*$^{-/-}$ mice (Figure 9(e)) with intensity-specific differences observed at some frequencies in post hoc comparisons. Overall, these data suggest that at high frequencies, there is a significant reduction in Peak I latencies in *CX3CR1*$^{-/-}$ mice, and this effect is propagated along the ascending auditory pathway. Further, *CX3CR1*$^{-/-}$ mice display decreased central conductivity time, as observed by decreased interpeak latencies.

Peak amplitude was determined as the level of deviation (μV) from the preceding trough to the apex of the relative peak (Figure 8 (a)). Compared to WT mice, *CX3CR1*$^{-/-}$ mice exhibited normal Peak I amplitude responses at most frequencies. At 4 kHz, genotype effects showed that there was a significantly elevated amplitude in the *CX3CR1*$^{-/-}$; however, *post hoc* analyses did not reveal intensity-specific differences. Genotype effects also showed that there was a small significant decrease in Peak I amplitude at 8 kHz and 32 kHz; however, multiple comparison analyses did not reveal significant differences at any intensity level tested (Figure 10(a)). *CX3CR1*$^{-/-}$ mice showed mostly normal Peaks II and III amplitude responses. Significant decreases in amplitude based on genotype effects were detected only at 8 kHz; however, multiple comparison analysis did not reveal significant intensity-specific differences (Figure 10(b,c)). Peak IV amplitudes were significantly reduced in *CX3CR1*$^{-/-}$ mice at 4, 12, and 16 kHz, but post hoc analyses did not reveal intensity-specific differences (Figure 10(d)). Together, these results show that *CX3CR1*$^{-/-}$ mice show slightly diminished ABR amplitudes.

4 | DISCUSSION

In the present study, we used a *CX3CR1* transgenic mouse line to investigate the role of fractalkine signaling in auditory circuit development. We found that disruption of fractalkine

signaling pathway led to increased expression of GLYT2 in the MNTB. Unlike our previous observations following microglia elimination, we found that loss of *CX3CR1* did not impair calyceal monoinnervation of MNTB neurons and led to an increase rather than a decrease in the expression levels of the mature astrocyte marker GFAP. Within the MNTB, *CX3CR1*$^{-/-}$ mice displayed loss of tonotopic size gradients of principal neurons as of their calyceal inputs. Functionally, ABR thresholds appeared normal; however, decreased latencies, especially for the highest frequency responses, were observed.

4.1 | Fractalkine function in regulation of synaptic protein expression

4.1.1 | Excitatory signaling in MNTB—

Principal neurons of MNTB receive large and fast neural excitatory input through the encapsulating calyx of Held (Borst & Soria van Hoeve, 2012; Forsythe, 1994; Held, 1893; Kuwabara et al., 1991; Tolbert & Morest, 1982). It was previously shown that VGLUT2 immunoreactivity in MNTB did not change between ages P6 and P14 in FVB mice (Rotschafer & Cramer, 2017). We found no age-related change in VGLUT1/2 expression levels in MNTB of WT mice, similar to our previous findings (Milinkeviciute et al., 2019). Although VGLUT1/2 expression was significantly lower in mutant mice at P8, it reached control levels by P14. Studies have shown that fractalkine signaling is involved in the postnatal functional development of excitatory synapses (Basilico et al., 2019; Hoshiko et al., 2012; Paolicelli et al., 2011; Zhan et al., 2014). We did not find an effect on VGLUT1/2 labeling in MNTB after hearing onset. This finding could be attributable to the microglial functional heterogeneity in different parts of the brain (Jacobs et al., 2019; Tan et al., 2020) at different time points during development (Li et al., 2019; Masuda et al., 2019; Ritzel et al., 2015). The difference in VGLUT1/2 levels at P8 could be attributable to a delay in maturation of synaptic terminals and/or an accelerated rate of synaptic pruning. However, calyces from WT and *CX3CR1*$^{-/-}$ animals appear to become comparable in terms of VGLUT1/2 expression as they grow and mature. After hearing onset we did not find any difference between VGLUT1/2 levels or calyceal surface area or shape factor. Together, our findings suggest a developmental function for *CX3CR1* in synaptic maturation in MNTB before hearing onset. *CX3CR1* signaling through microglia is needed for establishing early levels of VGLUT1/2, but in the absence of *CX3CR1* other mechanisms likely compensate for the deficit as the system matures.

4.1.2 | Inhibitory signaling in MNTB during early postnatal development—

We used two markers, VGAT and GLYT2, to investigate inhibitory synapses in MNTB. Previously, it was shown that *CX3CR1*$^{-/-}$ mice have significantly higher levels of VGAT puncta in the spinal cord, indicating a role for CX3CR1 in inhibitory synapse removal (Freria et al., 2017). We found that VGAT levels did not differ in the MNTB between mutant and wild type animals at P8 or P14, and only WT mice showed an age-related decrease in VGAT expression. In contrast, a significant increase in GLYT2 expression was seen at P14 in *CX3CR1*$^{-/-}$ animals when compared to age matched controls. The difference between VGAT and GLYT2 results may be due to the fact that the VGAT antibody labels both GABA- and GLYT2-positive inhibitory terminals (Chaudhry et al., 1998; Wang et al., 2009). The contribution of GABA expression to the overall VGAT areal coverage is unclear. GLYT2-positive puncta are found in MNTB before hearing onset (Friauf et al., 1999; Geal-Dor et al., 1993; Uziel et al., 1981). MNTB receives intrinsic inhibitory projections

(Kuwabara & Zook, 1991); however, the main source of inhibitory input is the VNTB (Albrecht et al., 2014). GLYT2 development is characterized by an initial increase of expression with a subsequent decrease after P10 and establishment of adult-like pattern by P22 in rats (Friauf et al., 1999). Taken together, our findings show impairment of GLYT2 development in mutant mice. We found that in *CX3CR1*$^{-/-}$ mice, GLYT2 expression was decreased in LSO, which receives inhibitory input from MNTB and excitatory input from AVCN. MNTB cells showed enhanced GLYT2 expression in *CX3CR1*$^{-/-}$ mice, while LSO showed less. In addition, GLYT2 expression in AVCN appeared to be reduced in *CX3CR1*$^{-/-}$ mice when compared to controls at 9 weeks. Reduced GLYT2 in AVCN may indicate reduced inhibition to the GBCs that project to MNTB principal neurons and/or to the spherical bushy cells that project to LSO. Together, these factors could greatly alter relative levels of inhibition and excitation in LSO in *CX3CR1*$^{-/-}$ mice. The effects of these alterations on the computation of interaural intensity differences and sound localization remain to be determined.

Fractalkine signaling has been previously shown to function in synaptic pruning during development. *CX3CR1*$^{-/-}$ mice showed increased synaptic engulfment in hippocampus during the second and the third postnatal weeks (Paolicelli et al., 2011). In contrast, loss of *CX3CR1* did not influence the pruning of excess climbing fibers and had no impact on the development of functional parallel fiber and inhibitory synapses with Purkinje cells in the cerebellar cortex (Kaiser et al., 2020). We found an age-related decrease in GLYT2 expression in WT animals but not in *CX3CR1*$^{-/-}$ mice, which may reflect loss of pruning of inhibitory synapses in MNTB in mutants. While our data showed increased GLYT2 in the MNTB at P14, at 9 weeks GLYT2-positive puncta appeared denser and aggregated. In LSO and VCN GLYT2 expression visually appeared sparser than in WT animals. It thus appears that fractalkine signaling regulates inhibitory protein expression and pruning differently in individual auditory brainstem nuclei.

It is possible that aberrant distribution of inhibitory terminals in MNTB is related to modifications in extracellular matrix (ECM) proteins. Recently, microglia were linked to the regulation of perineuronal net (PNN) formation and integrity (Crapser et al., 2020). Aggrecan, an ECM protein associated with PNNs, was shown to be important in the neurotransmission of inhibitory interneurons in the dentate gyrus (Yamada & Jinno, 2017) and PNNs regulate inhibitory perisomatic input in the prefrontal cortex (Carceller et al., 2020). Additionally, aggrecan was significantly increased in the granule layer of dentate gyrus in *CX3CR1*$^{-/-}$ mice (Bolos et al., 2018). MNTB neurons are inhibitory (Kuwabara & Zook, 1991; Tollin, 2003), parvalbumin positive (Felmy & Schneggenburger, 2004), and surrounded by PNNs consisting of various ECM proteins including aggrecan (Blosa et al., 2013; Blosa et al., 2015; Hartig et al., 2001). Disruption of PNNs in MNTB was shown to reduce excitability by enhancing the inhibition (Balmer, 2016). The possibility that PNN composition is related to synaptic changes in MNTB remains to be explored (Schmidt et al., 2020).

4.2 | *CX3CR1* in synaptic pruning

Microglia and astrocytes both contribute to developmental synaptic and axonal pruning to establish appropriate neural circuits (Bialas & Stevens, 2012; Peri & Nusslein-Volhard, 2008; Schafer et al., 2012; Schafer & Stevens, 2013). However, *CX3CR1* is only expressed by microglia that bind fractalkine (CX3CL1) produced by neurons (Harrison et al., 1998; Hatori et al., 2002; Jung et al., 2000) and developing oligodendrocyte progenitor cells (OPCs), which gets downregulated in mature oligodendrocytes (Zhang et al., 2014). Given CX3CL1-*CX3CR1* contributions to microglial migration (Cardona et al., 2006; Liang et al., 2009; Ruitenberg et al., 2008), it is possible that loss of fractalkine signaling prevents microglia from reaching the points of synaptic pruning or leads to a delay in microglial recruitment (Hoshiko et al., 2012). However, it seems unlikely because microglia are present in MNTB at P8 and P14 in mutant mice (Dinh et al., 2014).

4.3 | Fractalkine signaling in microglia–astrocyte communication

We previously found that elimination of microglia led to decreased expression of the mature astrocyte marker GFAP. Here, we found that the *CX3CR1* mutation led to increased expression of GFAP. These results together suggest that microglia regulate astrocyte maturation in multiple ways. Microglia, astrocytes, and neurons can influence each other's development and actions by regulating migration (Arno et al., 2014), proliferation rates (Antony et al., 2011; Walton et al., 2006), phagocytosis of precursor cells (Cunningham et al., 2013) and regulation of developmental switch from neuro- to astrogenesis (Bechade et al., 2011; Peunova & Enikolopov, 1995). Microglia may regulate astrocyte differentiation (Dalmau et al., 1997). Microglial depletion in cortical precursor cell cultures resulted in a reduction of newly generated astrocytes (Antony et al., 2011). Moreover, microglia secrete several molecules that influence astrocytic differentiation and/or proliferation (Bechade et al., 2011; Giulian et al., 1988; Nakanishi et al., 2007). In contrast, some literature suggests that astrocytes are present before microglial maturation and ramification takes place (Rezaie et al., 2002). In this way, astrocytes would contribute to microglial maturation (Navascues et al., 2000; Rezaie et al., 2002; Tanaka & Maeda, 1996). This idea is strengthened by the fact that astrocytes can stimulate proliferation of microglia (Frei et al., 1986; Lee et al., 1994). We found that GFAP expression is significantly increased in the absence of fractalkine signaling at P14. *CX3CR1* is not expressed by astrocytes (Harrison et al., 1998; Hatori et al., 2002; Jung et al., 2000); therefore, we suggest that the observed effect is due to disrupted fractalkine signaling between neurons and microglia, which in turn influence astrocyte maturation or regulate their numbers. The specific downstream signaling pathways remain to be identified.

4.4 | Microglia-neuron communication in the establishment of tonotopic gradients

Structures within the auditory system are tonotopically organized (Friauf, 1992; Kandler et al., 2009; Spirou et al., 1993). The development of tonotopic maps relies on spontaneous activity (Clause et al., 2014; Clause et al., 2017; Di Guilmi et al., 2019; Muller et al., 2019) as well as on other molecular cues (Karmakar et al., 2017; Macova et al., 2019; Miko et al., 2007). Various genes are differentially expressed along the tonotopic axis (Brew & Forsythe, 2005; Leao et al., 2006; Sato et al., 2009; Son et al., 2012). In MNTB, high-to-low best

frequencies are encoded in the medial-to-lateral axis (Sommer et al., 1993; Tolnai et al., 2008). Neurons also vary along the mediolateral axis of MNTB based on their response properties (Brew & Forsythe, 2005; Tolnai et al., 2008). Anatomically, cells located in the medial part of MNTB are smaller than those found in the lateral side. Thus, there is a neuronal size gradient along the mediolateral MNTB axis (Rotschafer & Cramer, 2017; Weatherstone et al., 2017). Our analysis shows that this size gradient is lost in the absence of fractalkine signaling at P14. The tonotopic size gradient becomes more pronounced in 9-week-old mutant mice; however, it still remains significantly different from that seen in WT mice. In addition, we described the size differences of calyces of Held between those located in the medial and lateral portions of the nucleus. Thus, CX3CL1-CX3CR1 signaling appears to be a communication pathway required for the establishment of tonotopic gradients in MNTB. Loss of CX3CR1 results in the loss of neuronal and calyceal size gradients, possibly through reciprocal signaling to principal neurons of MNTB as well as GBCs in AVCN.

4.5 | Fractalkine signaling effect on ABR wave latency

Our studies revealed that ABRs in *CX3CR1*$^{-/-}$ mice showed normal thresholds, slightly diminished peak amplitudes and reduced latencies, especially for the highest frequency stimulus tested (32 kHz). Loss of *CX3CR1* reduced the latencies of all four peaks, suggesting that the fractalkine signaling affects the entire ascending auditory chain rather than a particular region within the auditory pathway. Reduced ABR Peaks I and II latencies and interpeak I–II and II–III latencies have also been reported in maternal mice when compared to nulliparous mice suggestive of plasticity at the level of the VIIIth nerve and cochlear nucleus (Miranda et al., 2014).

An intriguing observation in our study was that the most significant alterations in the ABR recordings were seen in response to high frequencies, which could be related to the observed increases in cell body and calyx size in the medial portion of MNTB. The decrease in ABR latencies may also be due to changes in myelination of axons. Recently, it was shown that *CX3CR1*$^{-/-}$ mice display reduced engulfment of OPCs in the corpus callosum, and consequently increased numbers of oligodendrocytes and impaired myelination without any effect on axon numbers or their diameter. Surprisingly, the myelin sheath was thinner in mutant animals despite the elevated numbers of oligodendrocytes (Nemes-Baran et al., 2020). A thinner myelin sheath should decrease signal transmission, which would result in longer ABR latencies (Long et al., 2018; Naito et al., 1999; Zhou et al., 1995). Our observation of shorter latencies would suggest a thicker myelin sheath or larger axon diameters and shorter internodes (Ford et al., 2015). Interestingly, blocking CX3CR1 reversed demyelination in global cerebral ischemia and promoted differentiation and maturation of oligodendrocyte progenitor cells in hippocampus (Du et al., 2020). Again, these differences may be due to the temporal and spatial heterogeneity of microglia and their functions (Masuda et al., 2019; Tan et al., 2020).

There are limited data on the *CX3CR1*$^{-/-}$ phenotypes in the auditory system. So far, reports mainly focus on fractalkine signaling in the cochlea in response to injury, which was shown to be critical for hair cell and spiral ganglion neuron survival (Kaur et al., 2015; Kaur et al., 2018; Sato et al., 2010). *CX3CR1*$^{-/-}$ mice displayed enhanced synaptic degeneration in the

cochlea after moderate noise trauma. Similar to our results, authors reported no difference in auditory thresholds between WT and *CX3CR1*$^{-/-}$ mice prior to noise trauma (Kaur et al., 2019). Our anatomical studies, together with our central ABR peak latency data, suggest that CX3CR1 influences development of the brainstem auditory pathways.

4.6 | Concluding remarks

We have characterized projections to MNTB and auditory function in mice lacking the fractalkine receptor CX3CR1. While our previous study suggests that microglia are needed for pruning at the calyx of Held and for astrocyte maturation, the present study suggests that fractalkine signaling does not account for these roles. Instead, CX3CR1 appears to contribute distinct functions to auditory development. These functions may be more focused on inhibitory synaptic pruning and on tonotopic maps in MNTB. These findings highlight the dynamic functions of microglia in multiple aspects of auditory brainstem maturation.

Supplementary Material

Refer to Web version on PubMed Central for supplementary material.

ACKNOWLEDGMENTS

The authors thank Minhan L. Dinh and Sarah E. Rotschafer for assistance with pilot studies. The authors thank Dr. Adeela Syed at the Optical Biology Core Facility of the Developmental Biology Center at the University of California, Irvine, for her advice and help with confocal imaging and analysis. This work was supported by NIH R01 DC010796 and NIH T32 010775. This study was made possible in part through access to the Optical Biology Core Facility of the Developmental Biology Center, a shared resource supported by the Cancer Center Support Grant (CA-62203) and Center for Complex Biological Systems Support Grant (GM-076516) at the University of California, Irvine.

Funding information

National Institute on Deafness and Other Communication Disorders, Grant/Award Numbers: R01 DC010796, T32 DC010775

Abbreviations:

ABR	auditory brainstem recording
AVCN	anteroventral cochlear nucleus
ECM	extracellular matrix
EGFP	enhanced green fluorescent protein
GABA	gamma-aminobutyric acid
GBC	globular bushy cell
GFAP	glial fibrillary acidic protein
GLYT2	glycine transporter 2
MNTB	medial nucleus of the trapezoid body
OPC	oligodendrocyte progenitor cell

PNN	perineuronal net
RDA	rhodamine dextran amine
ROI	region of interest
VCN	ventral cochlear nucleus
VGAT	vesicular GABA transporter
VGLUT1/2	vesicular glutamate transporters 1/2
VNTB	ventral nucleus of trapezoid body

REFERENCES

Albrecht O, Dondzillo A, Mayer F, Thompson JA, & Klug A. (2014). Inhibitory projections from the ventral nucleus of the trapezoid body to the medial nucleus of the trapezoid body in the mouse. Front Neural Circuits, 8, 83. [PubMed: 25120436]

Antony JM, Paquin A, Nutt SL, Kaplan DR, & Miller FD (2011). Endogenous microglia regulate development of embryonic cortical precursor cells. Journal of Neuroscience Research, 89(3), 286–298. [PubMed: 21259316]

Armsen W, Himmel B, Betz H, & Eulenburg V. (2007). The C-terminal PDZ-ligand motif of the neuronal glycine transporter GlyT2 is required for efficient synaptic localization. Molecular and Cellular Neurosciences, 36(3), 369–380. [PubMed: 17851090]

Arno B, Grassivaro F, Rossi C, Bergamaschi A, Castiglioni V, Furlan R, Greter M, Favaro R, Comi G, Becher B, Martino G, & Muzio L. (2014). Neural progenitor cells orchestrate microglia migration and positioning into the developing cortex. Nature Communications, 5, 5611.

Awatramani GB, Turecek R, & Trussell LO (2005). Staggered development of GABAergic and glycinergic transmission in the MNTB. Journal of Neurophysiology, 93(2), 819–828. [PubMed: 15456797]

Balmer TS (2016). Perineuronal nets enhance the excitability of fast-spiking neurons. eNeuro, 3(4), ENEUR0.0112-ENEU16.2016.

Basilico B, Pagani F, Grimaldi A, Cortese B, di Angelantonio S, Weinhard L, Gross C, Limatola C, Maggi L, & Ragozzino D. (2019). Microglia shape presynaptic properties at developing glutamatergic synapses. Glia, 67(1), 53–67. [PubMed: 30417584]

Bechade C, Pascual O, Triller A, & Bessis A. (2011). Nitric oxide regulates astrocyte maturation in the hippocampus: Involvement of NOS2. Molecular and Cellular Neurosciences, 46(4), 762–769. [PubMed: 21354308]

Bergsman JB, De Camilli P, & McCormick DA (2004). Multiple large inputs to principal cells in the mouse medial nucleus of the trapezoid body. Journal of Neurophysiology, 92(1), 545–552. [PubMed: 15212444]

Bialas AR, & Stevens B. (2012). Glia: Regulating synaptogenesis from multiple directions. Current Biology, 22(19), R833–R835. [PubMed: 23058800]

Blosa M, Sonntag M, Bruckner G, Jager C, Seeger G, Matthews RT, Rubsamen R, Arendt T, & Morawski M. (2013). Unique features of extracellular matrix in the mouse medial nucleus of trapezoid body--implications for physiological functions. Neuroscience, 228, 215–234. [PubMed: 23069754]

Blosa M, Sonntag M, Jager C, Weigel S, Seeger J, Frischknecht R, Seidenbecher CI, Matthews RT, Arendt T, Rubsamen R, & Morawski M. (2015). The extracellular matrix molecule brevican is an integral component of the machinery mediating fast synaptic transmission at the calyx of Held. The Journal of Physiology, 593(19), 43414360.

Bogaerts S, Clements JD, Sullivan JM, & Oleskevich S. (2009). Automated threshold detection for auditory brainstem responses: Comparison with visual estimation in a stem cell transplantation study. BMC Neuroscience, 10, 104. [PubMed: 19706195]

Bolos M, Perea JR, Terreros-Roncal J, Pallas-Bazarra N, Jurado-Arjona J, Avila J, & Llorens-Martin M. (2018). Absence of microglial CX3CR1 impairs the synaptic integration of adult-born hippocampal granule neurons. Brain, Behavior, and Immunity, 68, 76–89.

Borst JG, & Soria van Hoeve J. (2012). The calyx of Held synapse: From model synapse to auditory relay. Annual Review of Physiology, 74, 199–224.

Brew HM, & Forsythe ID (2005). Systematic variation of potassium current amplitudes across the tonotopic axis of the rat medial nucleus of the trapezoid body. Hearing Research, 206(1–2), 116–132. [PubMed: 16081003]

Carceller H, Guirado R, Ripolles-Campos E, Teruel-Marti V, & Nacher J. (2020). Perineuronal nets regulate the inhibitory perisomatic input onto parvalbumin interneurons and gamma activity in the prefrontal cortex. The Journal of Neuroscience, 40(26), 5008–5018. [PubMed: 32457072]

Cardona AE, Pioro EP, Sasse ME, Kostenko V, Cardona SM, Dijkstra IM, Huang D, Kidd G, Dombrowski S, Dutta R, Lee JC, Cook DN, Jung S, Lira SA, Littman DR, & Ransohoff RM (2006). Control of microglial neurotoxicity by the fractalkine receptor. Nature Neuroscience, 9(7), 917–924. [PubMed: 16732273]

Chang A, Chen P, Guo S, Xu N, Pan W, Zhang H, Li C, & Tang J. (2018). Specific influences of early acoustic environments on Cochlear hair cells in postnatal mice. Neural Plasticity, 2018, 5616930.

Chaudhry FA, Reimer RJ, Bellocchio EE, Danbolt NC, Osen KK, Edwards RH, & Storm-Mathisen J. (1998). The vesicular GABA transporter, VGAT, localizes to synaptic vesicles in sets of glycinergic as well as GABAergic neurons. The Journal of Neuroscience, 18(23), 9733–9750. [PubMed: 9822734]

Clause A, Kim G, Sonntag M, Weisz CJ, Vetter DE, Rubsamen R, & Kandler K. (2014). The precise temporal pattern of prehearing spontaneous activity is necessary for tonotopic map refinement. Neuron, 82 (4), 822–835. [PubMed: 24853941]

Clause A, Lauer AM, & Kandler K. (2017). Mice lacking the Alpha9 subunit of the nicotinic acetylcholine receptor exhibit deficits in frequency difference limens and sound localization. Frontiers in Cellular Neuroscience, 11, 167. [PubMed: 28663725]

Crapser JD, Ochaba J, Soni N, Reidling JC, Thompson LM, & Green KN (2020). Microglial depletion prevents extracellular matrix changes and striatal volume reduction in a model of Huntington's disease. Brain, 143(1), 266–288. [PubMed: 31848580]

Cunningham CL, Martinez-Cerdeno V, & Noctor SC (2013). Microglia regulate the number of neural precursor cells in the developing cerebral cortex. The Journal of Neuroscience, 33(10), 4216–4233. [PubMed: 23467340]

Dalmau I, Finsen B, Tonder N, Zimmer J, Gonzalez B, & Castellano B. (1997). Development of microglia in the prenatal rat hippocampus. The Journal of Comparative Neurology, 377(1), 70–84. [PubMed: 8986873]

de Hoff RT (1978). Stereological uses of the area tangent count. In Miles RE & Serra J. (Eds.), Geometrical probability and biological structures: Buffon's 200th anniversary (pp. 99–113). Springer-Verlag.

Di Guilmi MN, Boero LE, Castagna VC, Rodriguez-Contreras A, Wedemeyer C, Gomez-Casati ME, & Elgoyhen AB (2019). Strengthening of the efferent olivocochlear system leads to synaptic dysfunction and tonotopy disruption of a central auditory nucleus. The Journal of Neuroscience, 39(36), 7037–7048. [PubMed: 31217330]

Dinh ML, Koppel SJ, Korn MJ, & Cramer KS (2014). Distribution of glial cells in the auditory brainstem: Normal development and effects of unilateral lesion. Neuroscience, 278, 237–252. [PubMed: 25158674]

Du B, Liang M, Zheng H, Fan C, Zhang H, Lu X, Du Z, Lian Y, Zhang Y, & Bi X. (2020). Anti-mouse CX3CR1 antibody alleviates cognitive impairment, neuronal loss and myelin deficits in an animal model of brain ischemia. Neuroscience, 438, 169–181. [PubMed: 32417340]

Felmy F, & Schneggenburger R. (2004). Developmental expression of the Ca2+−binding proteins calretinin and parvalbumin at the calyx of Held of rats and mice. The European Journal of Neuroscience, 20(6), 1473–1482. [PubMed: 15355314]

Ford MC, Alexandrova O, Cossell L, Stange-Marten A, Sinclair J, Kopp-Scheinpflug C, Pecka M, Attwell D, & Grothe B. (2015). Tuning of Ranvier node and internode properties in myelinated axons to adjust action potential timing. Nature Communications, 6, 8073.

Forsythe ID (1994). Direct patch recording from identified presynaptic terminals mediating glutamatergic EPSCs in the rat CNS, in vitro. The Journal of Physiology, 479(Pt 3), 381–387. [PubMed: 7837096]

Frei K, Bodmer S, Schwerdel C, & Fontana A. (1986). Astrocyte-derived interleukin 3 as a growth factor for microglia cells and peritoneal macrophages. Journal of Immunology, 137(11), 3521–3527.

Fremeau RT Jr., Troyer MD, Pahner I, Nygaard GO, Tran CH, Reimer RJ, Bellocchio EE, Fortin D, Storm-Mathisen J, & Edwards RH (2001). The expression of vesicular glutamate transporters defines two classes of excitatory synapse. Neuron, 31(2), 247–260. [PubMed: 11502256]

Freria CM, Hall JC, Wei P, Guan Z, McTigue DM, & Popovich PG (2017). Deletion of the Fractalkine receptor, CX3CR1, improves endogenous repair, axon sprouting, and synaptogenesis after spinal cord injury in mice. The Journal of Neuroscience, 37(13), 3568–3587. [PubMed: 28264978]

Friauf E. (1992). Tonotopic order in the adult and developing auditory system of the rat as shown by c-fos immunocytochemistry. The European Journal of Neuroscience, 4(9), 798–812. [PubMed: 12106303]

Friauf E, Aragon C, Lohrke S, Westenfelder B, & Zafra F. (1999). Developmental expression of the glycine transporter GLYT2 in the auditory system of rats suggests involvement in synapse maturation. The Journal of Comparative Neurology, 412(1), 17–37. [PubMed: 10440707]

Geal-Dor M, Freeman S, Li G, & Sohmer H. (1993). Development of hearing in neonatal rats: Air and bone conducted ABR thresholds. Hearing Research, 69(1–2), 236–242. [PubMed: 8226345]

Giulian D, Young DG, Woodward J, Brown DC, & Lachman LB (1988). Interleukin-1 is an astroglial growth factor in the developing brain. The Journal of Neuroscience, 8(2), 709–714. [PubMed: 3257519]

Gomes FC, Paulin D, & Moura NV (1999). Glial fibrillary acidic protein (GFAP): Modulation by growth factors and its implication in astrocyte differentiation. Brazilian Journal of Medical and Biological Research, 32 (5), 619–631. [PubMed: 10412574]

Harrison JK, Jiang Y, Chen S, Xia Y, Maciejewski D, McNamara RK, Streit WJ, Salafranca MN, Adhikari S, Thompson DA, Botti P, Bacon KB, & Feng L. (1998). Role for neuronally derived fractalkine in mediating interactions between neurons and CX3CR1-expressing microglia. Proceedings of the National Academy of Sciences of the United States of America, 95(18), 10896–10901. [PubMed: 9724801]

Hartig W, Singer A, Grosche J, Brauer K, Ottersen OP, & Bruckner G. (2001). Perineuronal nets in the rat medial nucleus of the trapezoid body surround neurons immunoreactive for various amino acids, calcium-binding proteins and the potassium channel subunit Kv3.1b. Brain Research, 899(1–2), 123–133. [PubMed: 11311873]

Hatori K, Nagai A, Heisel R, Ryu JK, & Kim SU (2002). Fractalkine and fractalkine receptors in human neurons and glial cells. Journal of Neuroscience Research, 69(3), 418–426. [PubMed: 12125082]

Held H. (1893). Die centrale Gehorleitung. Archiv fur Anatomie und Physiologie, Anatomische Abteilung, 17, 201–248.

Henry KR (1979). Auditory brainstem volume-conducted responses: Origins in the laboratory mouse. Journal of the American Auditory Society, 4(5), 173–178. [PubMed: 511644]

Herzog E, Bellenchi GC, Gras C, Bernard V, Ravassard P, Bedet C, Gasnier B, Giros B, & El Mestikawy S. (2001). The existence of a second vesicular glutamate transporter specifies subpopulations of glutamatergic neurons. The Journal of Neuroscience, 21 (22), RC181.

Hirose K, Discolo CM, Keasler JR, & Ransohoff R. (2005). Mononuclear phagocytes migrate into the murine cochlea after acoustic trauma. The Journal of Comparative Neurology, 489(2), 180–194. [PubMed: 15983998]

Hoffpauir BK, Grimes JL, Mathers PH, & Spirou GA (2006). Synaptogenesis of the calyx of Held: Rapid onset of function and one-to-one morphological innervation. The Journal of Neuroscience, 26(20), 5511–5523. [PubMed: 16707803]

Holcomb PS, Hoffpauir BK, Hoyson MC, Jackson DR, Deerinck TJ, Marrs GS, Dehoff M, Wu J, Ellisman MH, & Spirou GA (2013). Synaptic inputs compete during rapid formation of the calyx of Held: A new model system for neural development. The Journal of Neuroscience, 33(32), 12954–12969. [PubMed: 23926251]

Hoshiko M, Arnoux I, Avignone E, Yamamoto N, & Audinat E. (2012). Deficiency of the microglial receptor CX3CR1 impairs postnatal functional development of thalamocortical synapses in the barrel cortex. The Journal of Neuroscience, 32(43), 15106–15111. [PubMed: 23100431]

Ison JR, Allen PD, & O'Neill WE (2007). Age-related hearing loss in C57BL/6J mice has both frequency-specific and non-frequency-specific components that produce a hyperacusis-like exaggeration of the acoustic startle reflex. Journal of the Association for Research in Otolaryngology, 8(4), 539–550. [PubMed: 17952509]

Jacobs AJ, Castillo-Ruiz A, Cisternas CD, & Forger NG (2019). Microglial depletion causes region-specific changes to developmental neuronal cell death in the mouse brain. Developmental Neurobiology, 79(8), 769–779. [PubMed: 31207134]

Jewett DL, Romano MN, & Williston JS (1970). Human auditory evoked potentials: Possible brain stem components detected on the scalp. Science, 167(3924), 1517–1518. [PubMed: 5415287]

Jewett DL, & Williston JS (1971). Auditory-evoked far fields averaged from the scalp of humans. Brain, 94(4), 681–696. [PubMed: 5132966]

Jung S, Aliberti J, Graemmel P, Sunshine MJ, Kreutzberg GW, Sher A, & Littman DR (2000). Analysis of fractalkine receptor CX(3) CR1 function by targeted deletion and green fluorescent protein reporter gene insertion. Molecular and Cellular Biology, 20(11), 4106–4114. [PubMed: 10805752]

Kaiser N, Patz C, Brachtendorf S, Eilers J, & Bechmann I. (2020). Undisturbed climbing fiber pruning in the cerebellar cortex of CX3 CR1-deficient mice. Glia, 68(11), 2316–2329. [PubMed: 32488990]

Kandler K, Clause A, & Noh J. (2009). Tonotopic reorganization of developing auditory brainstem circuits. Nature Neuroscience, 12(6), 711–717. [PubMed: 19471270]

Kaneko T, Fujiyama F, & Hioki H. (2002). Immunohistochemical localization of candidates for vesicular glutamate transporters in the rat brain. The Journal of Comparative Neurology, 444(1), 39–62. [PubMed: 11835181]

Karmakar K, Narita Y, Fadok J, Ducret S, Loche A, Kitazawa T, Genoud C, Di Meglio T, Thierry R, Bacelo J, Luthi A, & Rijli FM (2017). Hox2 genes are required for tonotopic map precision and sound discrimination in the mouse auditory brainstem. Cell Reports, 18 (1), 185–197. [PubMed: 28052248]

Kaur T, Clayman AC, Nash AJ, Schrader AD, Warchol ME, & Ohlemiller KK (2019). Lack of Fractalkine receptor on macrophages impairs spontaneous recovery of ribbon synapses after moderate noise trauma in C57BL/6 mice. Frontiers in Neuroscience, 13, 620. [PubMed: 31263398]

Kaur T, Ohlemiller KK, & Warchol ME (2018). Genetic disruption of fractalkine signaling leads to enhanced loss of cochlear afferents following ototoxic or acoustic injury. The Journal of Comparative Neurology, 526(5), 824–835. [PubMed: 29218724]

Kaur T, Zamani D, Tong L, Rubel EW, Ohlemiller KK, Hirose K, & Warchol ME (2015). Fractalkine signaling regulates macrophage recruitment into the cochlea and promotes the survival of spiral ganglion neurons after selective hair cell lesion. The Journal of Neuroscience, 35(45), 15050–15061. [PubMed: 26558776]

Kuwabara N, DiCaprio RA, & Zook JM (1991). Afferents to the medial nucleus of the trapezoid body and their collateral projections. The Journal of Comparative Neurology, 314(4), 684–706. [PubMed: 1816271]

Kuwabara N, & Zook JM (1991). Classification of the principal cells of the medial nucleus of the trapezoid body. The Journal of Comparative Neurology, 314(4), 707–720. [PubMed: 1816272]

Leao RN, Sun H, Svahn K, Berntson A, Youssoufian M, Paolini AG, Fyffe RE, & Walmsley B. (2006). Topographic organization in the auditory brainstem of juvenile mice is disrupted in congenital deafness. The Journal of Physiology, 571(Pt 3), 563–578. [PubMed: 16373385]

Lee SC, Liu W, Brosnan CF, & Dickson DW (1994). GM-CSF promotes proliferation of human fetal and adult microglia in primary cultures. Glia, 12(4), 309–318. [PubMed: 7890333]

Li Q, Cheng Z, Zhou L, Darmanis S, Neff NF, Okamoto J, Gulati G, Bennett ML, Sun LO, Clarke LE, Marschallinger J, Yu G, Quake SR, Wyss-Coray T, & Barres BA (2019). Developmental heterogeneity of microglia and brain myeloid cells revealed by deep single-cell RNA sequencing. Neuron, 101(2), 207–223.e210.

Liang KJ, Lee JE, Wang YD, Ma W, Fontainhas AM, Fariss RN, & Wong WT (2009). Regulation of dynamic behavior of retinal microglia by CX3CR1 signaling. Investigative Ophthalmology & Visual Science, 50(9), 4444–4451. [PubMed: 19443728]

Liu YY, Ju G, & Wong-Riley MT (2001). Distribution and colocalization of neurotransmitters and receptors in the pre-Botzinger complex of rats. Journal of Applied Physiology (Bethesda, MD: 1985), 91 (3), 1387–1395.

Long P, Wan G, Roberts MT, & Corfas G. (2018). Myelin development, plasticity, and pathology in the auditory system. Developmental Neurobiology, 78(2), 80–92. [PubMed: 28925106]

Lowery RL, Tremblay ME, Hopkins BE, & Majewska AK (2017). The microglial fractalkine receptor is not required for activity-dependent plasticity in the mouse visual system. Glia, 65(11), 17441761.

Macova I, Pysanenko K, Chumak T, Dvorakova M, Bohuslavova R, Syka J, Fritzsch B, & Pavlinkova G. (2019). Neurod1 is essential for the primary Tonotopic organization and related auditory information processing in the midbrain. The Journal of Neuroscience, 39(6), 984–1004. [PubMed: 30541910]

Masuda T, Sankowski R, Staszewski O, Bottcher C, Amann L, Sagar SC, Nessler S, Kunz P, van Loo G, Coenen VA, Reinacher PC, Michel A, Sure U, Gold R, Grun D, Priller J, Stadelmann C, & Prinz M. (2019). Spatial and temporal heterogeneity of mouse and human microglia at single-cell resolution. Nature, 566 (7744), 388–392. [PubMed: 30760929]

Mayer F, Albrecht O, Dondzillo A, & Klug A. (2014). Glycinergic inhibition to the medial nucleus of the trapezoid body shows prominent facilitation and can sustain high levels of ongoing activity. Journal of Neurophysiology, 112(11), 2901–2915. [PubMed: 25185813]

McIntire SL, Reimer RJ, Schuske K, Edwards RH, & Jorgensen EM (1997). Identification and characterization of the vesicular GABA transporter. Nature, 389(6653), 870–876. [PubMed: 9349821]

Miko IJ, Nakamura PA, Henkemeyer M, & Cramer KS (2007). Auditory brainstem neural activation patterns are altered in EphA4- and ephrin-B2-deficient mice. The Journal of Comparative Neurology, 505 (6), 669–681. [PubMed: 17948875]

Milinkeviciute G, Henningfield CM, Muniak MA, Chokr SM, Green KN, & Cramer KS (2019). Microglia regulate pruning of specialized synapses in the auditory brainstem. Front Neural Circuits, 13, 55. [PubMed: 31555101]

Miranda JA, Shepard KN, McClintock SK, & Liu RC (2014). Adult plasticity in the subcortical auditory pathway of the maternal mouse. PLoS One, 9(7), e101630.

Miyamoto A, Wake H, Ishikawa AW, Eto K, Shibata K, Murakoshi H, Koizumi S, Moorhouse AJ, Yoshimura Y, & Nabekura J. (2016). Microglia contact induces synapse formation in developing somatosensory cortex. Nature Communications, 7, 12540.

Muller NIC, Sonntag M, Maraslioglu A, Hirtz JJ, & Friauf E. (2019). Topographic map refinement and synaptic strengthening of a sound localization circuit require spontaneous peripheral activity. The Journal of Physiology, 597, 5469–5493. [PubMed: 31529505]

Muniak MA, Ayeni FE, & Ryugo DK (2018). Hidden hearing loss and endbulbs of Held: Evidence for central pathology before detection of ABR threshold increases. Hearing Research, 364, 104–117. [PubMed: 29598838]

Naito R, Murofushi T, Mizutani M, & Kaga K. (1999). Auditory brainstem responses, electrocochleograms, and cochlear microphonics in the myelin deficient mutant hamster ‘bt’. Hearing Research, 136(1–2), 44–48. [PubMed: 10511623]

Nakanishi M, Niidome T, Matsuda S, Akaike A, Kihara T, & Sugimoto H. (2007). Microglia-derived interleukin-6 and leukaemia inhibitory factor promote astrocytic differentiation of neural stem/progenitor cells. The European Journal of Neuroscience, 25(3), 649–658. [PubMed: 17328769]

Navascues J, Calvente R, Marin-Teva JL, & Cuadros MA (2000). Entry, dispersion and differentiation of microglia in the developing central nervous system. Anais da Academia Brasileira de Ciências, 72(1), 91–102. [PubMed: 10932110]

Nelson LH, & Lenz KM (2017). Microglia depletion in early life programs persistent changes in social, mood-related, and locomotor behavior in male and female rats. Behavioural Brain Research, 316, 279–293. [PubMed: 27613230]

Nemes-Baran AD, White DR, & DeSilva TM (2020). Fractalkinedependent microglial pruning of viable Oligodendrocyte progenitor cells regulates myelination. Cell Reports, 32(7), 108047.

Neniskyte U, & Gross CT (2017). Errant gardeners: Glial-cell-dependent synaptic pruning and neurodevelopmental disorders. Nature Reviews. Neuroscience, 18(11), 658–670. [PubMed: 28931944]

Nimmerjahn A, Kirchhoff F, & Helmchen F. (2005). Resting microglial cells are highly dynamic surveillants of brain parenchyma in vivo. Science, 308(5726), 1314–1318. [PubMed: 15831717]

Nonaka S, & Nakanishi H. (2019). Microglial clearance of focal apoptotic synapses. Neuroscience Letters, 707, 134317.

Ohlemiller KK, Jones SM, & Johnson KR (2016). Application of mouse models to research in hearing and balance. Journal of the Association for Research in Otolaryngology, 17(6), 493–523. [PubMed: 27752925]

Paolicelli RC, Bolasco G, Pagani F, Maggi L, Scianni M, Panzanelli P, Giustetto M, Ferreira TA, Guiducci E, Dumas L, Ragozzino D, & Gross CT (2011). Synaptic pruning by microglia is necessary for normal brain development. Science, 333(6048), 1456–1458. [PubMed: 21778362]

Parkhurst CN, Yang G, Ninan I, Savas JN, Yates JR, Lafaille JJ, Hempstead BL, Littman DR, & Gan WB (2013). Microglia promote learning-dependent synapse formation through brain-derived neurotrophic factor. Cell, 155(7), 1596–1609. [PubMed: 24360280]

Peri F, & Nusslein-Volhard C. (2008). Live imaging of neuronal degradation by microglia reveals a role for v0-ATPase a1 in phagosomal fusion in vivo. Cell, 133(5), 916–927. [PubMed: 18510934]

Peunova N, & Enikolopov G. (1995). Nitric oxide triggers a switch to growth arrest during differentiation of neuronal cells. Nature, 375 (6526), 68–73. [PubMed: 7536899]

Picton TW, Hillyard SA, Krausz HI, & Galambos R. (1974). Human auditory evoked potentials I. Evaluation of components. Electroencephalogr Clin Neurophysiol, 36(2), 179–190. [PubMed: 4129630]

Reemst K, Noctor SC, Lucassen PJ, & Hol EM (2016). The indispensable roles of microglia and astrocytes during brain development. Frontiers in Human Neuroscience, 10, 566. [PubMed: 27877121]

Reshef R, Kudryavitskaya E, Shani-Narkiss H, Isaacson B, Rimmerman N, Mizrahi A, & Yirmiya R. (2017). The role of microglia and their CX3CR1 signaling in adult neurogenesis in the olfactory bulb. eLife, 6, e30809.

Rezaie P, Trillo-Pazos G, Greenwood J, Everall IP, & Male DK (2002). Motility and ramification of human fetal microglia in culture: An investigation using time-lapse video microscopy and image analysis. Experimental Cell Research, 274(1), 68–82. [PubMed: 11855858]

Ritzel RM, Patel AR, Pan S, Crapser J, Hammond M, Jellison E, & McCullough LD (2015). Age- and location-related changes in microglial function. Neurobiology of Aging, 36(6), 2153–2163. [PubMed: 25816747]

Rotschafer SE, & Cramer KS (2017). Developmental emergence of phenotypes in the auditory brainstem nuclei of Fmr1 knockout mice. eNeuro, 4(6). https://doi.org/ENEURO.0264-17.2017.

Ruitenberg MJ, Vukovic J, Blomster L, Hall JM, Jung S, Filgueira L, McMenamin PG, & Plant GW (2008). CX3CL1/fractalkine regulates branching and migration of monocyte-derived cells in the mouse olfactory epithelium. Journal of Neuroimmunology, 205(1–2), 80–85. [PubMed: 18951638]

Sato E, Shick HE, Ransohoff RM, & Hirose K. (2010). Expression of fractalkine receptor CX3CR1 on cochlear macrophages influences survival of hair cells following ototoxic injury. Journal of the Association for Research in Otolaryngology, 11(2), 223–234. [PubMed: 19936834]

Sato T, Doi K, Hibino H, & Kubo T. (2009). Analysis of gene expression profiles along the tonotopic map of mouse cochlea by cDNA microarrays. Acta Otolaryngol, 562, 12–17.

Schafer DP, Lehrman EK, Kautzman AG, Koyama R, Mardinly AR, Yamasaki R, Ransohoff RM, Greenberg ME, Barres BA, & Stevens B. (2012). Microglia sculpt postnatal neural circuits in an activity and complement-dependent manner. Neuron, 74(4), 691–705. [PubMed: 22632727]

Schafer DP, & Stevens B. (2013). Phagocytic glial cells: Sculpting synaptic circuits in the developing nervous system. Current Opinion in Neurobiology, 23(6), 1034–1040. [PubMed: 24157239]

Schafer DP, & Stevens B. (2015). Microglia function in central nervous system development and plasticity. Cold Spring Harbor Perspectives in Biology, 7(10), a020545.

Schindelin J, Arganda-Carreras I, Frise E, Kaynig V, Longair M, Pietzsch T, Preibisch S, Rueden C, Saalfeld S, Schmid B, Tinevez JY, White DJ, Hartenstein V, Eliceiri K, Tomancak P, & Cardona A. (2012). Fiji: An open-source platform for biological-image analysis. Nature Methods, 9(7), 676–682. [PubMed: 22743772]

Schmidt S, Arendt T, Morawski M, & Sonntag M. (2020). Neurocan contributes to perineuronal net development. Neuroscience, 442, 69–86. [PubMed: 32634529]

Schrode KM, Muniak MA, Kim YH, & Lauer AM (2018). Central compensation in auditory brainstem after damaging noise exposure. eNeuro, 5(4), ENEURO.0250-ENEU18.2018.

Sinclair JL, Fischl MJ, Alexandrova O, Hebeta M, Grothe B, Leibold C, & Kopp-Scheinpflug C. (2017). Sound-evoked activity influences myelination of brainstem axons in the trapezoid body. The Journal of Neuroscience, 37(34), 8239–8255. [PubMed: 28760859]

Sipe GO, Lowery RL, Tremblay ME, Kelly EA, Lamantia CE, & Majewska AK (2016). Microglial P2Y12 is necessary for synaptic plasticity in mouse visual cortex. Nature Communications, 7, 10905.

Sommer I, Lingenhohl K, & Friauf E. (1993). Principal cells of the rat medial nucleus of the trapezoid body: An intracellular in vivo study of their physiology and morphology. Experimental Brain Research, 95(2), 223–239. [PubMed: 8224048]

Son EJ, Wu L, Yoon H, Kim S, Choi JY, & Bok J. (2012). Developmental gene expression profiling along the tonotopic axis of the mouse cochlea. PLoS One, 7(7), e40735.

Sonntag M, Englitz B, Kopp-Scheinpflug C, & Rubsamen R. (2009). Early postnatal development of spontaneous and acoustically evoked discharge activity of principal cells of the medial nucleus of the trapezoid body: An in vivo study in mice. The Journal of Neuroscience, 29 (30), 9510–9520. [PubMed: 19641114]

Sousa C, Biber K, & Michelucci A. (2017). Cellular and molecular characterization of microglia: A unique immune cell population. Frontiers in Immunology, 8, 198. [PubMed: 28303137]

Spirou GA, May BJ, Wright DD, & Ryugo DK (1993). Frequency organization of the dorsal cochlear nucleus in cats. The Journal of Comparative Neurology, 329(1), 36–52. [PubMed: 8454725]

Sun S, Yu H, Yu H, Honglin M, Ni W, Zhang Y, Guo L, He Y, Xue Z, Ni Y, Li J, Feng Y, Chen Y, Shao R, Chai R, & Li H. (2015). Inhibition of the activation and recruitment of microglia-like cells protects against neomycin-induced ototoxicity. Molecular Neurobiology, 51(1), 252–267. [PubMed: 24781382]

Tan YL, Yuan Y, & Tian L. (2020). Microglial regional heterogeneity and its role in the brain. Molecular Psychiatry, 25(2), 351–367. [PubMed: 31772305]

Tanaka J, & Maeda N. (1996). Microglial ramification requires non-diffusible factors derived from astrocytes. Experimental Neurology, 137 (2), 367–375. [PubMed: 8635553]

Thompson AM, & Schofield BR (2000). Afferent projections of the superior olivary complex. Microscopy Research and Technique, 51(4), 330–354. [PubMed: 11071718]

Tolbert LP, & Morest DK (1982). The neuronal architecture of the anteroventral cochlear nucleus of the cat in the region of the cochlear nerve root: Electron microscopy. Neuroscience, 7(12), 3053–3067. [PubMed: 7162626]

Tollin DJ (2003). The lateral superior olive: A functional role in sound source localization. The Neuroscientist, 9(2), 127–143. [PubMed: 12708617]

Tolnai S, Hernandez O, Englitz B, Rubsamen R, & Malmierca MS (2008). The medial nucleus of the trapezoid body in rat: Spectral and temporal properties vary with anatomical location of the units. The European Journal of Neuroscience, 27(10), 2587–2598. [PubMed: 18547245]

Uziel A, Romand R, & Marot M. (1981). Development of cochlear potentials in rats. Audiology, 20(2), 89–100. [PubMed: 7224981]

Wake H, Moorhouse AJ, Jinno S, Kohsaka S, & Nabekura J. (2009). Resting microglia directly monitor the functional state of synapses in vivo and determine the fate of ischemic terminals. The Journal of Neuroscience, 29(13), 3974–3980. [PubMed: 19339593]

Walton NM, Sutter BM, Laywell ED, Levkoff LH, Kearns SM, Marshall GP, Scheffler B, & Steindler DA (2006). Microglia instruct subventricular zone neurogenesis. Glia, 54(8), 815–825. [PubMed: 16977605]

Wang Y, Kakizaki T, Sakagami H, Saito K, Ebihara S, Kato M, Hirabayashi M, Saito Y, Furuya N, & Yanagawa Y. (2009). Fluorescent labeling of both GABAergic and glycinergic neurons in vesicular GABA transporter (VGAT)-venus transgenic mouse. Neuroscience, 164(3), 1031–1043. [PubMed: 19766173]

Weatherstone JH, Kopp-Scheinpflug C, Pilati N, Wang Y, Forsythe ID, Rubel EW, & Tempel BL (2017). Maintenance of neuronal size gradient in MNTB requires sound-evoked activity. Journal of Neurophysiology, 117(2), 756–766. [PubMed: 27881722]

Whitelaw BS (2018). Microglia-mediated synaptic elimination in neuronal development and disease. Journal of Neurophysiology, 119(1), 1–4. [PubMed: 28835520]

Wimmer VC, Nevian T, & Kuner T. (2004). Targeted in vivo expression of proteins in the calyx of Held. Pflügers Archiv, 449(3), 319–333. [PubMed: 15452710]

Wolf SA, Boddeke HW, & Kettenmann H. (2017). Microglia in physiology and disease. Annual Review of Physiology, 79, 619–643.

Yamada J, & Jinno S. (2017). Molecular heterogeneity of aggrecan-based perineuronal nets around five subclasses of parvalbumin-expressing neurons in the mouse hippocampus. The Journal of Comparative Neurology, 525(5), 1234–1249. [PubMed: 27718219]

Zhan Y, Paolicelli RC, Sforazzini F, Weinhard L, Bolasco G, Pagani F, Vyssotski AL, Bifone A, Gozzi A, Ragozzino D, & Gross CT (2014). Deficient neuron-microglia signaling results in impaired functional brain connectivity and social behavior. Nature Neuroscience, 17(3), 400–406. [PubMed: 24487234]

Zhang Y, Chen K, Sloan SA, Bennett ML, Scholze AR, O'Keeffe S, Phatnani HP, Guarnieri P, Caneda C, Ruderisch N, Deng S, Liddelow SA, Zhang C, Daneman R, Maniatis T, Barres BA, & Wu JQ (2014). An RNA-sequencing transcriptome and splicing database of glia, neurons, and vascular cells of the cerebral cortex. The Journal of Neuroscience, 34(36), 11929–11947. [PubMed: 25186741]

Zhou R, Assouline JG, Abbas PJ, Messing A, & Gantz BJ (1995). Anatomical and physiological measures of auditory system in mice with peripheral myelin deficiency. Hearing Research, 88(1–2), 87–97. [PubMed: 8576008]

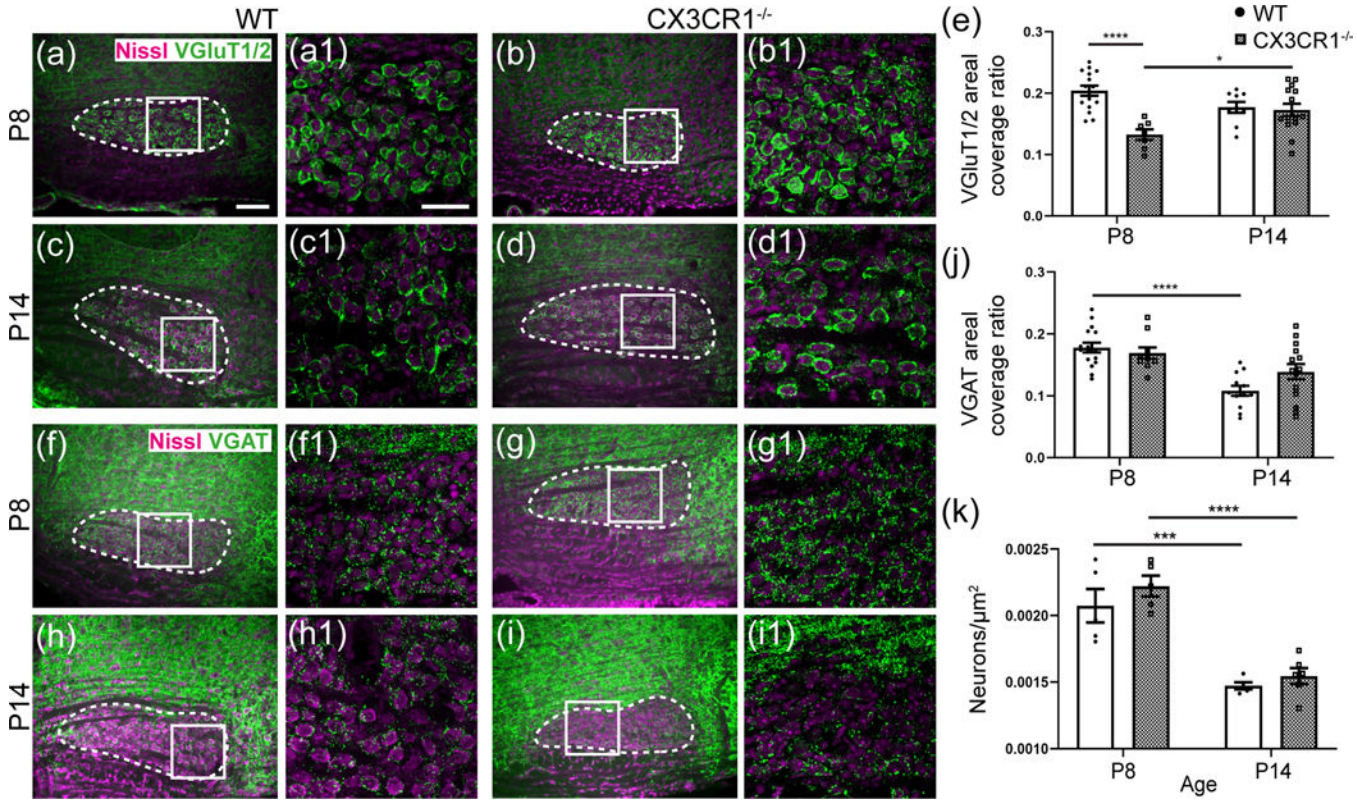

FIGURE 1.

Effects of fractalkine receptor mutation on vesicular glutamate transporters 1/2 (VGLUT1/2) and vesicular GABA transporter (VGAT) presynaptic protein expression in medial nucleus of the trapezoid body (MNTB). (a,b): Images of VGLUT1/2 immunolabel in MNTB from wild-type (WT) and *CX3CR1*$^{-/-}$ mice at P8. MNTB is indicated with a dashed line. Nissl-stained cell bodies are shown in magenta; VGLUT1/2 immunolabel is shown in green. (c,d) VGLUT1/2 immunofluorescence in MNTB in WT and *CX3CR1*$^{-/-}$ animals at P14. (a1-d1) Higher magnification confocal z-stack images of VGLUT1/2 staining in MNTB of (a-d). (e) Areal coverage ratio of VGLUT1/2 labeling in MNTB. There was significantly less VGLUT1/2 in mutant than in WT mice at P8. However, VGLUT1/2 levels significantly increased with age in *CX3CR1*$^{-/-}$ mice and there was no difference in VGLUT1/2 labeling between the two groups at P14. (f,g) Images of VGAT immunofluorescence in MNTB from control and mutant mice at P8. (h,i) VGAT staining in WT and *CX3CR1*$^{-/-}$ mice at P14. MNTB is indicated with a dashed line. Nissl-stained cell bodies are shown in magenta; VGAT labeling is shown in green. VGAT immunolabel is comparable but less abundant in both WT and *CX3CR1*$^{-/-}$ mice at P14. (f1-i1) Higher magnification confocal z-stack images of VGAT staining in MNTB of (f-i). (j) Areal coverage ratio of VGAT in MNTB. There was a significant decrease in VGAT labeling with age in WT mice but not in *CX3CR1*$^{-/-}$ mice. (k) Neuronal density in MNTB. Neuronal density was similar in both genotypes at P8 and P14. There was a significant age-related decrease in neuronal density in both groups. Scale bar in (a) = 200 µm, applies to panels (a-i). Scale bar in (al) = 50 µm, applies to panels (a1-i1)

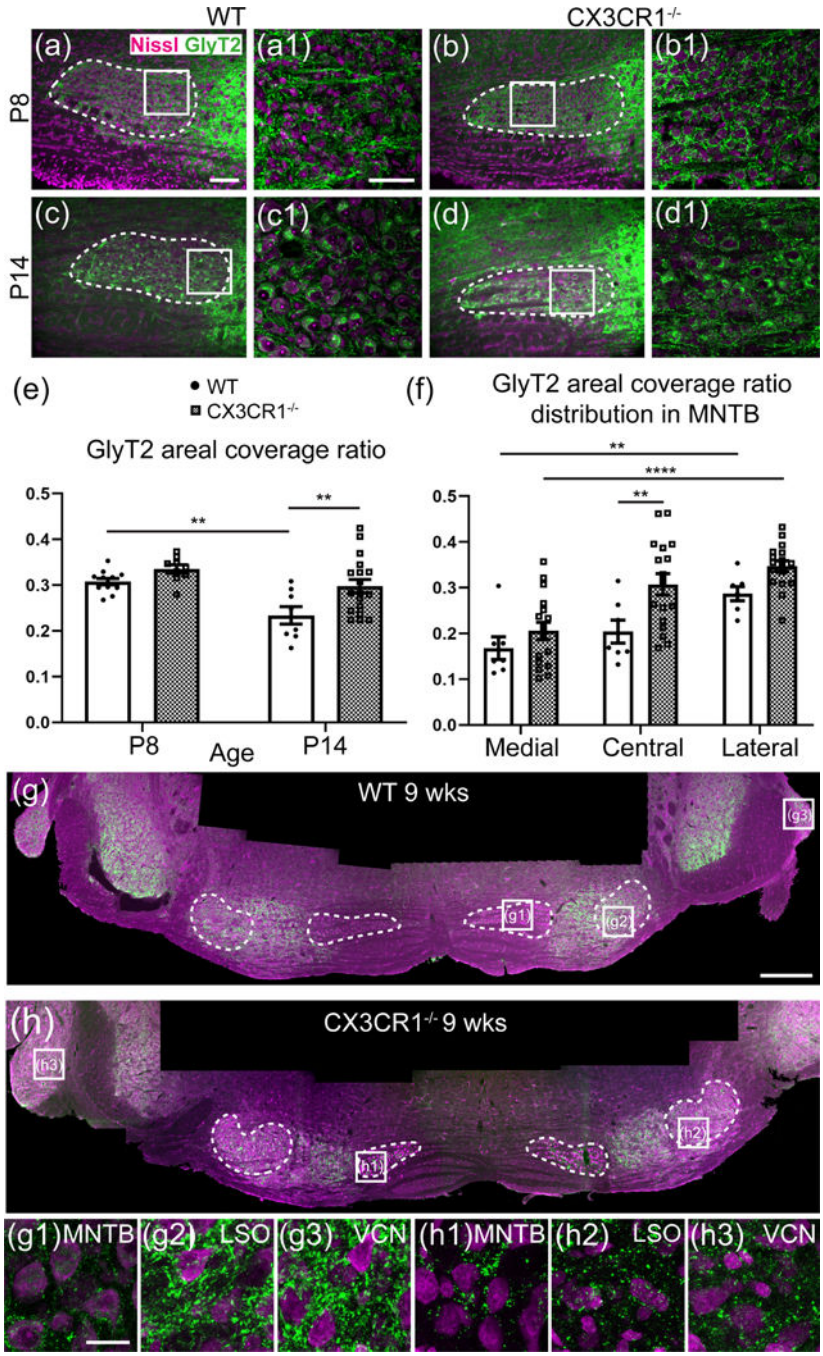

FIGURE 2.

Effects of *CX3CR1* mutation on glycine transporter 2 (GLYT2) expression in medial nucleus of the trapezoid body (MNTB). (a,b) GLYT2 immunolabeling in MNTB from WT and *CX3CR1*$^{-/-}$ mice at P8. (c,d) GLYT2 staining in MNTB from control and mutant mice at P14. Nissl-stained cell bodies are shown in magenta; GLYT2 labeling is shown in green. *CX3CR1*$^{-/-}$ animals exhibit visually stronger GLYT2 labeling than wild-type (WT) mice with more GLYT2-positive axons traversing MNTB (d). (a1-d1) Higher magnification confocal z-stack images of GLYT2 staining in MNTB of (a-d). (e) Quantified GLYT2 areal

coverage ratio in both genotypes at P8 and P14. We found an age-related significant decrease in GLYT2 coverage in wild-type (WT) group but not in mutants. At P14, *CX3CR1*$^{-/-}$ animals have significantly higher GLYT2 coverage than the control group. (f) Quantified GLYT2 areal coverage ratio in medial, central, and lateral divisions of MNTB at P14. There is significantly more GLYT2 in the lateral part of MNTB than medial in WT and mutant mice. There is significantly more GLYT2 in the middle portion of MNTB of *CX3CR1*$^{-/-}$ mice than WT mice. (g) GLYT2 immunolabel in the brainstem of WT mouse at 9 weeks. MNTB and LSO are outlined in dashed lines. (g1) A maximal projection of 63x confocal z-stack of GLYT2 immunolabel in MNTB. (g2) A maximal projection of 63x confocal z-stack of GLYT2 immunolabel in LSO. (g3) A maximal projection of 63x confocal z-stack of GLYT2 immunolabel in VCN. (g1-g3) Panels represent square frames in panel (g) designated with corresponding letters. (h) GLYT2 immunolabel in the brainstem of *CX3CR1*$^{-/-}$ mouse at 9 weeks. (h1), (h2), and (h3) represent a maximal projection of 63X confocal z-stack of GLYT2 immunolabel in MNTB, LSO and VCN of *CX3CR1*$^{-/-}$ mice, respectively and represent square frames in panel (h). Scale bar in (a) = 200 μm, applies to panels (a-d). Scale bar in (a1) = 50 μm applies to panels (a1-d1). Scale bar in (g) = 800 μm applies to panels (g) and (h). Scale bar in (g1) = 20 μm applies to panels (g1)-(h3)

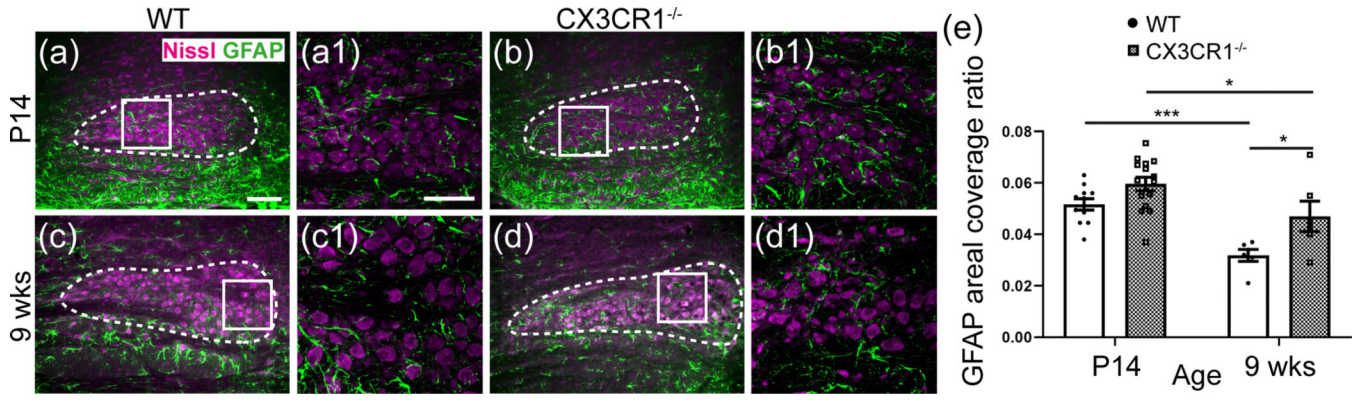

FIGURE 3.

Effects of fractalkine receptor mutation on glial fibrillary acidic protein (GFAP) expression in MNTB. (a,b) Medial nucleus of the trapezoid body (MNTB) (dashed line) from WT and *CX3CR1*$^{-/-}$ mice at P14 showing Nissl stain (magenta) and GFAP (green) expression. (c,d) GFAP immunolabel in MNTB of WT and *CX3CR1*$^{-/-}$ mice at 9 weeks. (a1-d1): Higher magnification confocal z-stack images of GFAP labeling in MNTB, represent square frames from panels (a-d). (e) Areal coverage ratio of GFAP in MNTB. GFAP coverage significantly decreases with age in WT and mutant animals. GFAP expression is significantly increased in *CX3CR1*$^{-/-}$ group at 9 weeks. Scale bar in (a) = 200 μm, applies to panels (a-d). Scale bar in (a1) = 50 μm, applies to panels (a1-d1)

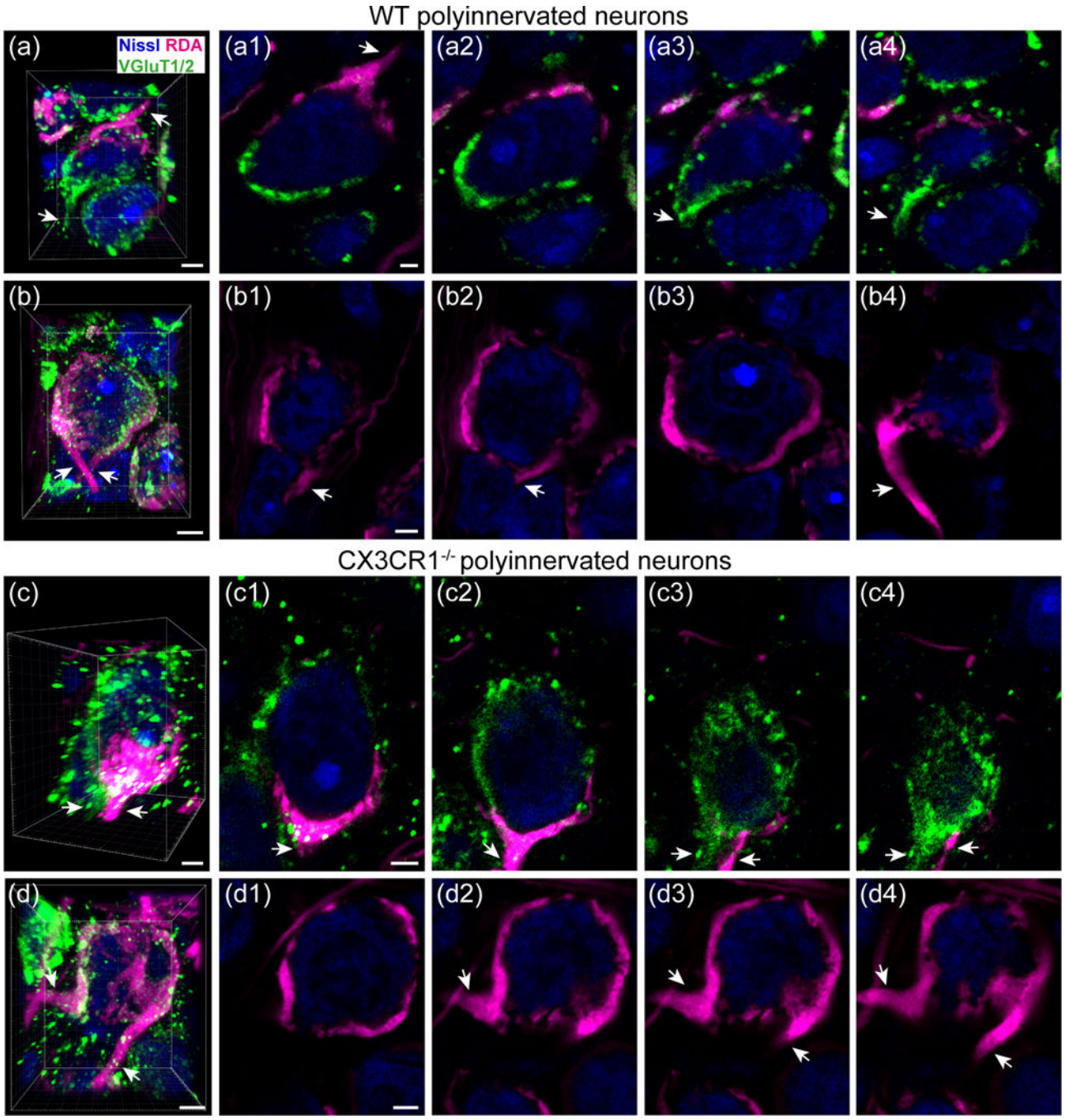

FIGURE 4.

Examples of polyinnervated neurons. (a) Polyinnervated neuron contacted by rhodamine dextran amine (RDA)-filled and vesicular glutamate transporters 1/2 (VGLUT1/2) positive calyx in MNTB of WT mouse at 9 weeks. Axons are indicated with white arrows. (a1-a4) Cross-sectional images of the neuron in (a). (b) Polyinnervated neuron in MNTB of WT mouse at 9 weeks contacted by two RDA-filled calyces. (b1-b4) Cross-sectional images of the neuron in (b). (c) Polyinnervated neuron contacted by RDA-filled and VGLUT1/2 positive calyx in MNTB of *CX3CR1*$^{-/-}$ mouse at 9 weeks. (c1-c4) Cross-sectional images of

the neuron in (c). (d) Polyinnervated neuron in MNTB of *CX3CR1*$^{-/-}$ mouse at 9 weeks contacted by two RDA-filled calyces. (d1-d4) Cross-sectional images of the neuron in (d). Scale bar in (a) = 4 μm, (a1) = 2 μm, applies to panels (a1-a3). Scale bar in (b) = 5 μm, (b1) = 3 μm, applies to panels (b1-b3). Scale bar in (c) = 3 μm, (c1) = 3 μm, applies to panels (c1-c3). Scale bar in (d) = 4 μm, (d1) = 3 μm, applies to panels (d1-d3)

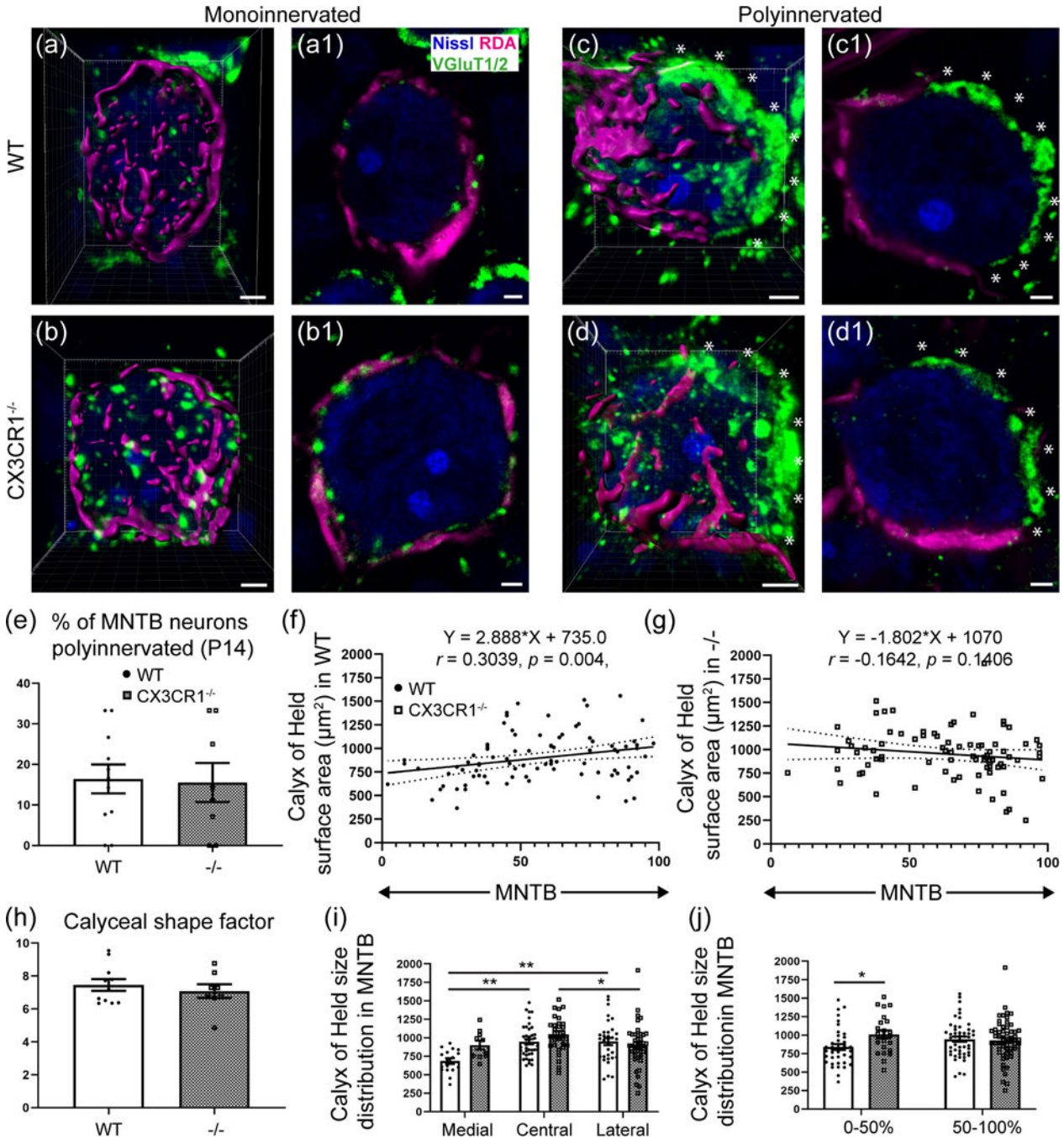

FIGURE 5.

Confocal analysis of polyinnervation. (a,b) Reconstructed rhodamine dextran amine (RDA)-labeled calyces of Held (magenta) terminating on medial nucleus of the trapezoid body (MNTB) principal neurons (blue) in a control (a) and a *CX3CR1*$^{-/-}$ mouse (b) at P14, respectively. Both are examples of monoinnervated MNTB neurons as evidenced by RDA-labeled calyces with no additional VGLUT1/2 (green) labeling outside of RDA-labeled calyces. (a1,b1) Cross-sectional images of neurons in (a) and (b). (c,d) Examples of polyinnervated neurons in WT (c) and *CX3CR1*$^{-/-}$ mouse (d) at P14 as evidenced by

VGLUT1/2 staining outside of RDA-labeled calyces (white asterisks). (c1,d1) Cross-sectional images of neurons in (c) and (d). (e) Percentage of neurons polyinnervated. There was no significant difference between WT and mutant mice at P14 in the percentage of polyinnervated MNTB neurons. (f) Correlation between the size and position of the calyx of Held in MNTB of WT mice at P14. (g) Correlation between the size and position of the calyx of Held in MNTB of mutant mice at P14. There is a significant correlation between the location of the calyx of Held and its surface area in the MNTB of WT but not in *CX3CR1*−/− mice. (h) Shape factor of calyces of Held in WT and mutant mice at P14 indicating no difference in complexity. (i) Surface area of calyces of Held in the medial, central and lateral parts of MNTB. There was no difference between surface area of calyces of Held between WT and $CX3CR1^{-/-}$ animals. (j) Surface area of calyces of Held in the medial and lateral halves of MNTB. Calyces are significantly larger in mutant than in WT mice in the medial half of MNTB. The difference in results in (i) and (j) depends on the way MNTB is subdivided and is mostly due to uneven number of calyces of Held analyzed in different parts of MNTB. Scale bars in (a-d) = 3 μm. Scale bars in (a1-d1) = 2 μm

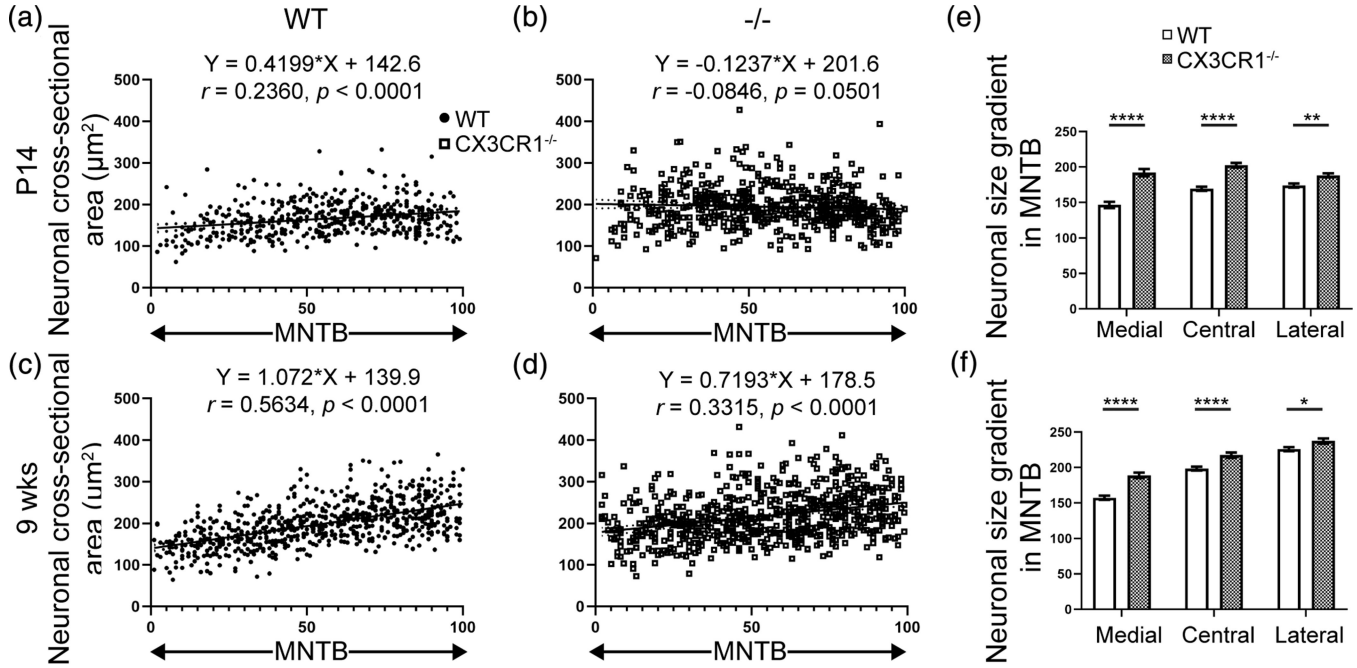

FIGURE 6.

Effects of fractalkine receptor mutation on neuronal cross-sectional size gradients in medial nucleus of the trapezoid body (MNTB). (a) Neuronal cross-sectional area distribution along the mediolateral axis in wild-type (WT) mice at P14. (b) The correlation between the position along the tonotopic axis and neuronal cross-sectional area in mutant mice at P14. The difference between the correlation coefficients of neuronal cross-sectional area in WT and mutant mice at P14 is significant. (c) Neuronal cross-sectional area distribution along the mediolateral axis in WT mice at 9 weeks. (d) The correlation between the position along the tonotopic axis and neuronal cross-sectional area in mutant mice at 9 weeks. The difference between the correlation coefficients of neuronal cross-sectional area in WT and mutant mice at 9 weeks is significant. There is a significant difference between the correlation coefficients of neuronal cross-sectional area *CX3CR1*$^{-/-}$ mice at P14 and 9 weeks. (e) Neuronal sizes in the medial, central, and lateral parts of MNTB in WT and *CX3CR1*$^{-/-}$ mice at P14. (f) Neuronal sizes in the medial, central, and lateral parts of MNTB in WT and *CX3CR1*$^{-/-}$ mice at P14. Bars represent all neurons measured from three MNTBs from three animals for each genotype. Mutant mice had significantly larger neurons in all subdivisions of MNTB

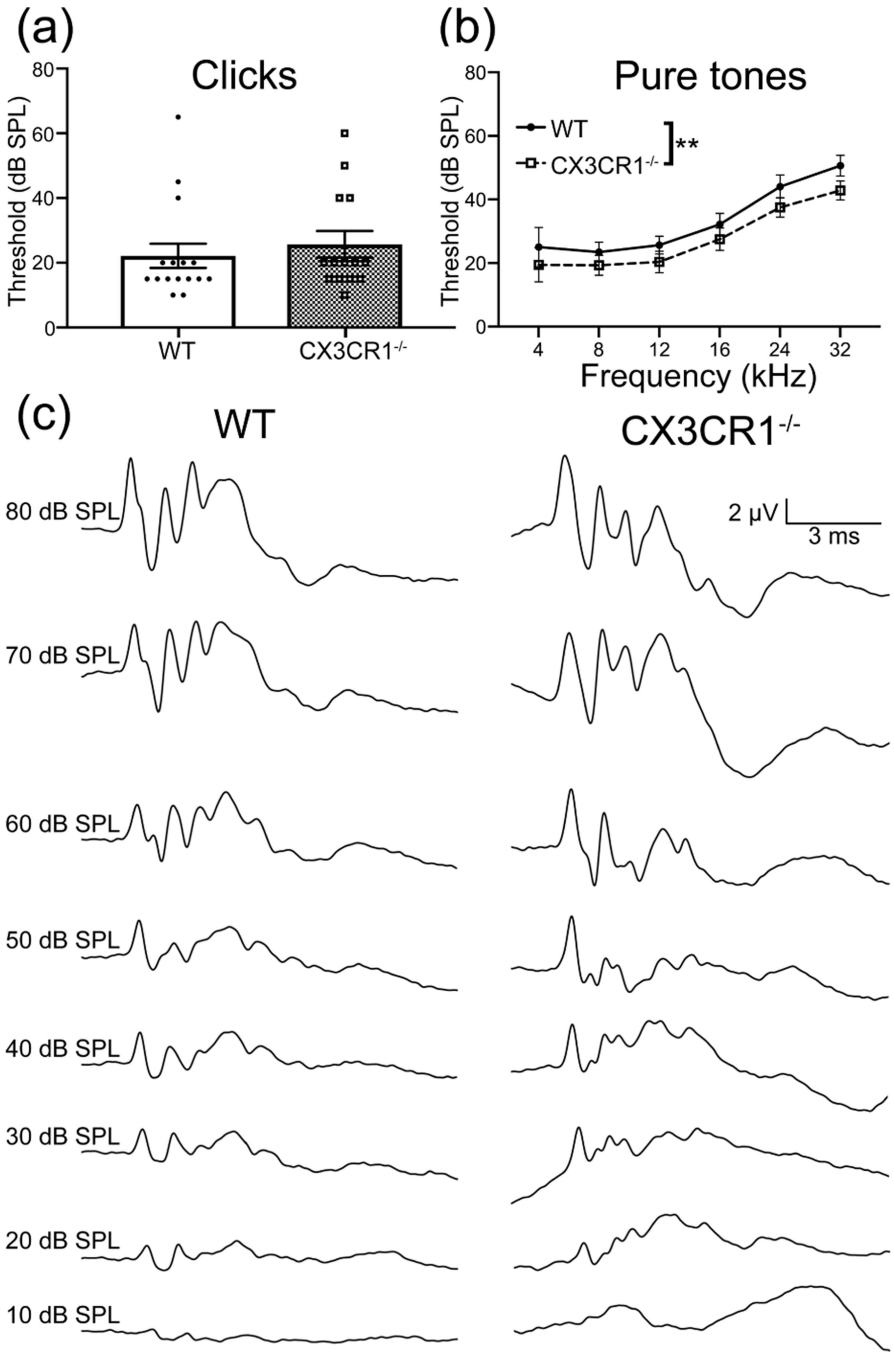

FIGURE 7.

Auditory thresholds are not affected by the loss of fractalkine signaling at 9 weeks of age. (a) Average thresholds for responses to click stimuli. (b) Average auditory thresholds for responses to tone stimuli. (c) Examples of wild-type (WT) and *CX3CR1*$^{-/-}$ mouse threshold traces in response to clicks. There is no difference between WT and *CX3CR1*$^{-/-}$ animals

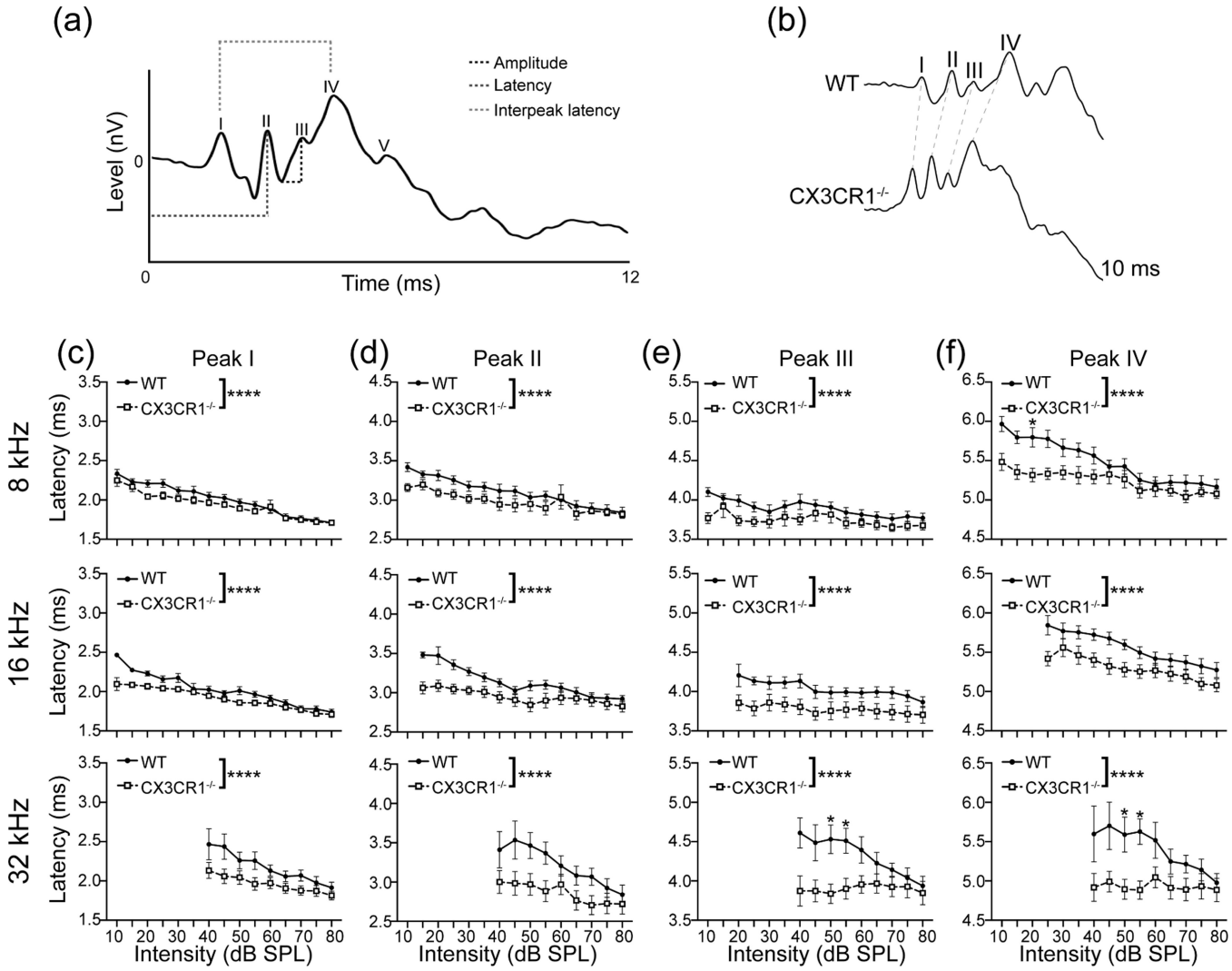

FIGURE 8.

Loss of fractalkine signaling leads to reduced auditory brainstem recording (ABR) peak latencies. (a) Schematics of ABR waveform. (b) ABR waveforms of WT and *CX3CR1*$^{-/-}$ group at 9 weeks of age. (c-f) Average latencies for Peaks I-IV in response to pure tone stimuli at 8, 16, and 32 kHz at 10–80 dB SPL. All peaks at all frequency levels (except for 4 kHz) in the *CX3CR1*$^{-/-}$ group showed significantly reduced latencies compared to WT

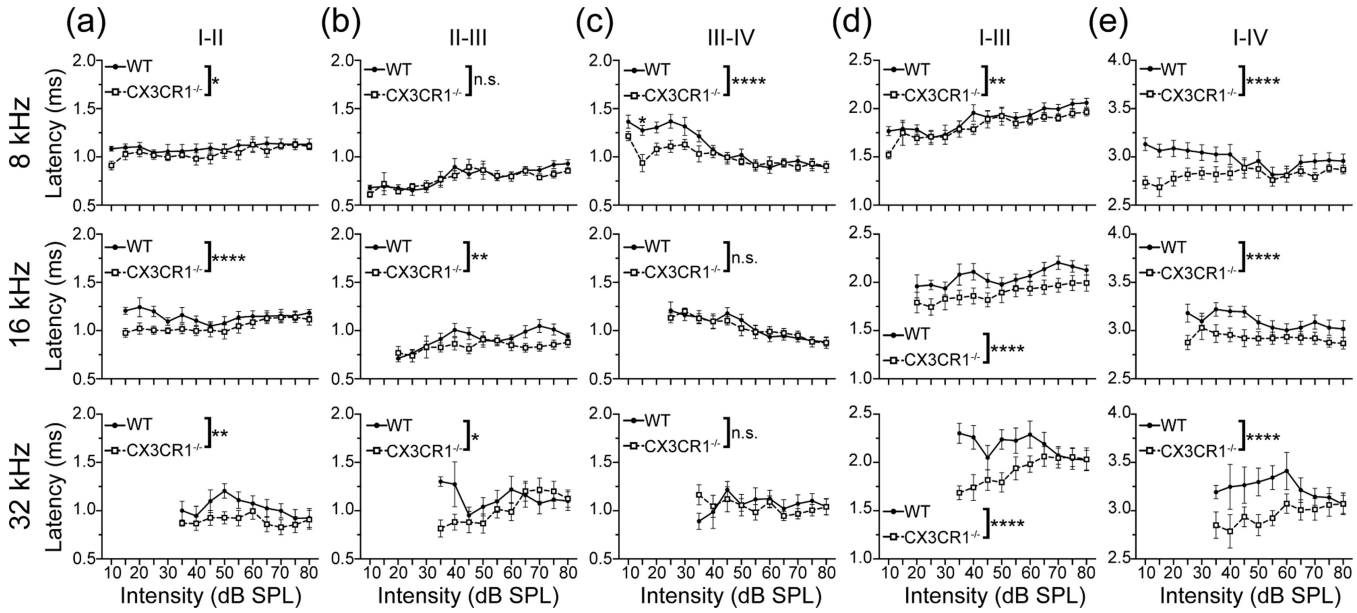

FIGURE 9.

CX3CR1$^{-/-}$ mice show altered central conductivity as measured by auditory brainstem recording (ABR) interpeak latencies. (a-e) Average interpeak latencies between Peaks I-II, II-III, III-IV, I-III, and I-IV in response to pure tone stimuli at 8,16, and 32 kHz in 5 dB SPL intervals between 10 and 80 dB SPL. Interpeak latencies between most peaks in *CX3CR1*$^{-/-}$ mice were reduced compared to WT mice at all frequency levels

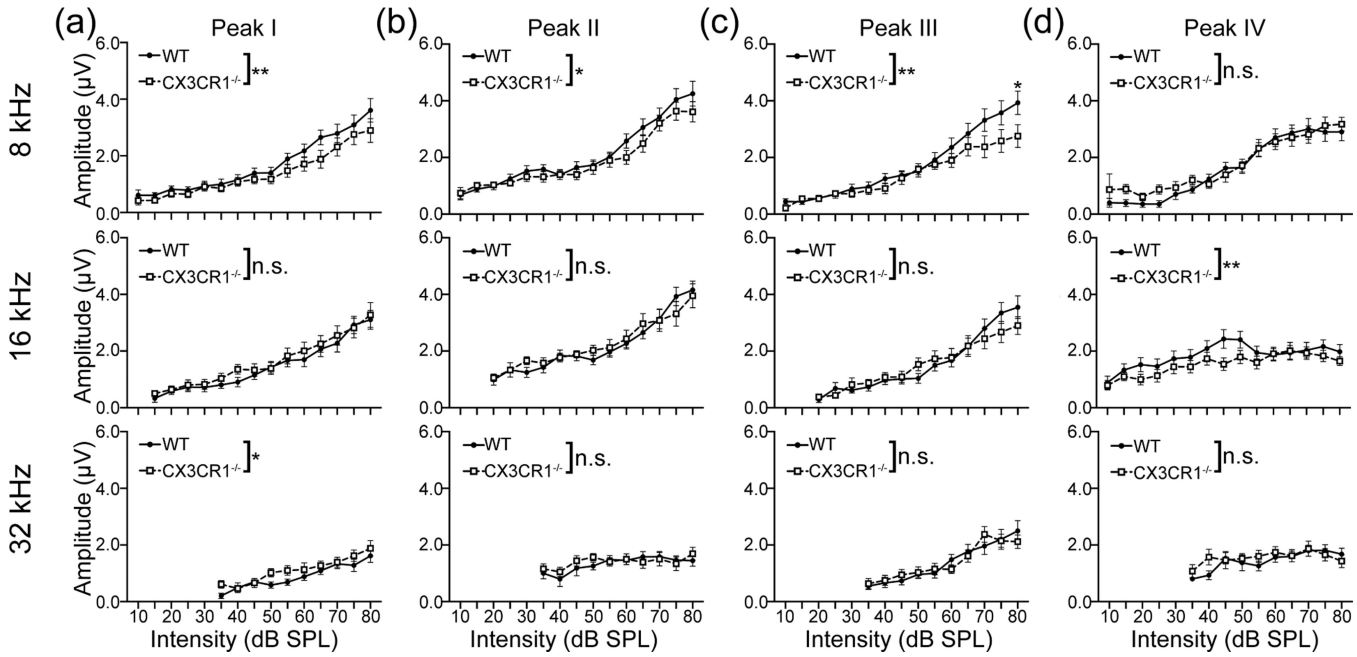

FIGURE 10.

ABR peak amplitudes are reduced in *CX3CR1*$^{-/-}$ mice in the lowest frequency tested. (a-d) Average peak I-IV amplitudes in response to pure tone stimuli at 8,16, and 32 kHz at 10–80 dB SPL. *CX3CR1*$^{-/-}$ mice show reduced amplitudes in Peaks I-III at 8 kHz and increased amplitudes at Peak I only in response to 32 kHz. Loss of fractalkine signaling does not affect peak amplitudes at 16 kHz or Peaks II-IV amplitudes at 32 kHz

TABLE 1

List of primary antibodies used in the project

Antigen	Host	RRID	Cat. no	Source	Dilution
GFAP	Chicken	AB_304558	ab4674	Abcam	1:1000
GlyT2	Rabbit	AB_2619997	272003	Synaptic Systems	1:200
VGAT	Rabbit	AB_2492282	2100-VGAT	PhosphoSolutions	1:200
VGluT1/2	Rabbit	AB_2285905	135503	Synaptic Systems	1:200

TABLE 2

Numbers of neurons and calyces of Held analyzed

Genotype	Animals used	Animal ID	Reconstructed neurons	Reconstructed calyces	Number of monoinnervated neurons	Number of poly-innervated neurons
wt	11	B276	8	15	11	4
		B277	1	6	5	1
		B278	3	14	11	3
		B280	0	6	4	2
		B281	2	12	11	1
		B282	2	10	10	0
		B664	6	16	13	3
		B665	1	13	12	1
		B668	4	7	7	0
		B670	0	7	6	1
		18–259	1	6	4	2
CX3CR1$^{-/-}$	8	18–197	5	14	12	2
		18–198	1	9	8	1
		18–201	5	17	17	0
		18–202	2	12	12	0
		18–255	1	9	6	3
		18–296	1	9	6	3
		18–297	6	12	9	3
		18–305	3	14	13	1